

JOYS: The [D/H] abundance derived from protostellar outflows across the Galactic disk measured with JWST

L. Francis¹, E. F. van Dishoeck^{1,3}, A. Caratti o Garatti⁶, M. L. van Gelder¹, C. Gieser^{3,2}, H. Beuther², T.P. Ray¹⁰
L. Tychoniec¹, P. Nazari⁴ S. Reyes² P. J. Kavanagh⁵, P. Klaassen⁷, M. Güdel^{8,2,9}, and T. Henning²

¹ Leiden Observatory, Leiden University, PO Box 9513, 2300 RA Leiden, The Netherlands

² Max Planck Institute for Extraterrestrial Physics, Gießenbachstraße 1, 85749 Garching bei München

³ Max Planck Institute for Astronomy, Königstuhl 17, 69117 Heidelberg, Germany

⁴ European Southern Observatory, Karl-Schwarzschild-Strasse 2, 85748 Garching bei München, Germany

⁵ Department of Experimental Physics, Maynooth University-National University of Ireland Maynooth, Maynooth, Co Kildare, Ireland

⁶ INAF-Osservatorio Astronomico di Capodimonte, Salita Moiarriello 16, I-80131 Napoli, Italy

⁷ UK Astronomy Technology Centre, Royal Observatory Edinburgh, Blackford Hill, Edinburgh EH9 3HJ, UK

⁸ Department of Astrophysics, University of Vienna, Türkenschanzstr. 17, 1180 Vienna, Austria

⁹ ETH Zürich, Institute for Particle Physics and Astrophysics, Wolfgang-Pauli-Str. 27, 8093 Zürich, Switzerland School of Cosmic Physics, Dublin Institute for Advanced Studies, 31 Fitzwilliam Place, Dublin 2, Ireland

ABSTRACT

Context. The total deuterium abundance [D/H] in the universe is set by just two processes: the creation of deuterium in Big Bang Nucleosynthesis at an abundance of $[D/H] = 2.58 \pm 0.13 \times 10^{-5}$, and its destruction within stellar interiors (astration). Measurements of variations in the total [D/H] abundance can thus potentially provide a probe of Galactic chemical evolution. However, most observational measurements of [D/H] are only sensitive to the gas-phase deuterium, and the amount of deuterium sequestered in dust grains is debated. With the launch of the James Webb Space Telescope (JWST), it is now possible to measure the gas-phase [D/H] at unprecedented sensitivity and distances through observation of mid-IR lines of H₂ and HD. Comparisons of gas-phase [D/H] with the constraints on the total [D/H] from the primordial abundance and Galactic chemical evolution models can provide insight into the degree of Deuterium lock-up in grains and the star formation history of our Galaxy.

Aims. We use data from the JWST Observations of Young protoStars (JOYS) program of 5 nearby and resolved low-mass protostellar outflows and 5 distant high-mass protostellar outflows taken with the JWST Mid Infrared Instrument (MIRI) Medium Resolution Spectrometer (MRS) to measure gas-phase [D/H] via H₂ and HD lines, assuming the gas is fully molecular.

Methods. We extract spectra from various locations in the outflows. Using a rotational diagram analysis covering lines of H₂ and HD with similar excitation energies, we derive the column density of HD and H₂ or their upper limits. We then calculate the gas-phase [D/H] from the column density results, and additionally apply a correction factor for the effect of chemical conversion of HD to atomic D and non-LTE excitation on the HD abundance in the shocks. To investigate the spatial distribution of the bulk gas and species refractory species associated with the dust grains, we also construct integrated line intensity maps of H₂, HD, [Fe II], [Fe I], and [S I] lines.

Results. A comparison of gas-phase [D/H] between our low-mass sources shows variations of up to a factor of ~ 4 , despite these sources likely having formed in nearly the same region of the Galactic disk that would be expected to have nearly constant total [D/H]. Most measurements of gas-phase [D/H] from our work or previous studies produce $[D/H] \leq 1.0 \times 10^{-5}$, a factor of 2 – 4 lower than found from local UV absorption lines and as expected from Galactic chemical evolution models. In the integrated line intensity maps, the morphology of the HD R(6) line emission is strongly correlated with the H₂ S(7), [S I], and [Fe I] lines which mostly trace high velocity jet knots and bright bow-shocks. In our extracted spectra along the outflows, there is similarly a strong correlation between the H₂ and HD column density and the [S I] and [Fe I] line flux, however, no correlation is seen between [D/H] and the [S I] or [Fe I] line flux.

Conclusions. The variations in [D/H] between our low-mass sources and the low [D/H] with respect to Galactic chemical evolution models suggest that our observations are not sensitive to the total [D/H]. Significant depletion of deuterium onto carbonaceous dust grains is a possible explanation, and tentative evidence of enhanced [D/H] towards positions with higher gas-phase Fe abundance is seen in the HH 211 outflow. Deeper observations of HD and H₂ across a wider range of shock conditions and modelling of the carbonaceous dust-grain destruction and shock conditions are warranted to test for the effects of depletion.

Key words. astrochemistry – stars – Galaxy: abundances – Infrared: ISM – ISM: jets and outflows – Stars: formation

1. Introduction

Deuterium is expected to only be created during Big Bang Nucleosynthesis (BBN). Afterwards, the deuterium abundance in the universe is depleted as it is incorporated into stellar interiors and burned into ³He in the process of astration (Epstein

et al. 1976). There is no known nucleosynthetic process to replenish the supply of deuterium, and thus the deuterium abundance with respect to hydrogen ([D/H]) has been proposed as a robust measure of stellar chemical evolution; with more generations of star formation, there should be an increasing destruction of deuterium by astration (Sarkar 1996). The primordial [D/H]

set by BBN has been accurately determined from UV observations of ultraviolet D I and H I absorption lines in high-redshift, metal-poor quasars to be $2.53 \pm 0.04 \times 10^{-5}$ (Cooke et al. 2014). This value of [D/H] is in good agreement with BBN model predictions based on cosmic microwave background observations of $2.58 \pm 0.13 \times 10^{-5}$ (Cyburt et al. 2016).

If [D/H] can be accurately measured in different locations through the Galactic disk, it should be an extremely valuable yet relatively simple probe of Galactic chemical evolution. Models of the formation of the Galactic disk generally predict that less star formation has occurred in the outer galaxy, and thus that [D/H] should increase with Galactocentric radius (R_{GC}) (e.g. Chiappini et al. 2002; Romano et al. 2003, 2006; van de Voort et al. 2018). This picture is complicated by other effects, such as the infall of pristine and deuterium-rich gas which has experienced little astration (Prantzos 1996; Romano et al. 2006; van de Voort et al. 2018), and infall from metal-rich/deuterium-depleted gas originating in winds driven by starbursts (Tsujiimoto et al. 2010; Tsujiimoto 2011). To date, however, there have been few direct constraints on [D/H] outside a few kpc from the Sun with which to constrain [D/H] throughout the Galaxy.

Early attempts at measuring [D/H] as a function of R_{GC} were made using radio-wavelength transitions of deuterated molecules such as DCN/HCN (Penzias et al. 1977; Penzias 1979), however, such surveys are now known to suffer from chemical fractionation effects which can alter the abundance of deuterated molecules by several orders of magnitude (Wooten 1987; Awad et al. 2014; Ceccarelli et al. 2014; Tielens 2013). To date, most measurements of [D/H] in our Galaxy come from UV absorption lines of D I and H I, however, their interpretation in terms of astration is debated (see Tosi 2010 for a review). Along sight lines with low total hydrogen column density within the local bubble ($\log(N_H) < 19.2 \text{ cm}^{-2}$), [D/H] is approximately constant at $1.5 \pm 0.4 \times 10^{-5}$, however, beyond the local bubble, variations of a factor of 4-5 in the derived [D/H] are seen between sight lines separated by only a few hundred pc (Linsky et al. 2006). Linsky et al. (2006) have argued that this variation is in fact the result of variations in the depletion of the gas-phase deuterium onto dust grains. Since the C-D bond is stronger than the D-H bond, it is energetically favorable for deuterium to replace hydrogen in carbonaceous dust grains or polycyclic aromatic hydrocarbons (PAHs, Jura 1982; Tielens 1983; Draine 2006; Tielens 2008). Indeed, the C-D bond of aromatic and aliphatic carbon molecules has been detected in emission (Peeters et al. 2004, 2024). Linsky et al. (2006) show that [D/H] along the different sightlines is anti-correlated with the depletion of different refractory elements (e.g. Fe, Si). Regions with a high [D/H] and low levels of depletion may recently have experienced erosion or destruction of dust grains from supernova shocks, thus releasing D back into the gas phase. A tentative correlation between [D/H] and the H_2 rotational temperature is also observed, which Linsky et al. (2006) suggest may be the result of clouds with warmer gas having a lower level of refractory depletion.

If depletion onto dust grains is significant, the highest [D/H] values observed are most representative of the total deuterium abundance in the local galactic disk. Taking dust depletion into account, a Bayesian analysis of the UV measurements suggest the corrected true [D/H] in the local Galactic disk is $\geq 2.0 \pm 0.1 \times 10^{-5}$ (Prodanović et al. 2010). This result is supported by recent updated measurements of [D/H] which have been improved with more precise H I measurements, although the correlation between refractory element depletion and [D/H] is somewhat weaker (Friedman et al. 2023). The depletion scenario has also been argued against by Hébrard (2010), who instead derive

[D/H] from measuring [D/O] with UV absorption lines of D I and O I, and then scaling by the ISM oxygen abundance. They find that [D/O] is in fact homogenous along a similar spread of sightlines, and suggest [D/H] of the local galactic disk may be a much lower value of $7 \pm 2 \times 10^{-6}$ instead. Regardless, UV absorption lines become impractical with distances from the Sun > 2.5 kpc due to blending of the D I/H I lines that occurs with a higher Hydrogen column density (Hoopes et al. 2003), increasing extinction in the Galactic plane, and the lack of bright background stars at large distances, and are thus also not well-suited to surveys over a wide range of R_{GC} .

An alternative simple probe of [D/H] is provided by mid- to far-infrared rotational lines of H_2 and HD, the simplest deuterated molecule. In the dense environments of molecular clouds, most deuterium should be in the form of HD, and the measurement of HD lines should provide direct and accurate means of obtaining the [D/H] ratio. As opposed to more complex deuterated species, chemical fractionation effects are not expected to be significant, though the chemical conversion of HD to atomic D can be important for abundance determination (Bertoldi et al. 1999). However, the HD molecule is difficult to observe in the mid-IR due to the low Einstein coefficients A_{ul} of order 10^{-5} s^{-1} relative to other IR-active species such as CO_2 ($A_{ul} \sim 1\text{-}100 \text{ s}^{-1}$), high upper energy levels ($E_{up} \geq 1900 \text{ K}$) requiring strong excitation conditions, and its low abundance relative to H_2 . Furthermore, rotational lines of HD are found in the mid to far-IR, and are not accessible from the ground. Only a handful of such HD detections have thus ever been made with the Infrared Space Observatory (ISO), *Spitzer*, and *Herschel*. All of these detections are in relatively nearby regions, either in shocks found in protostellar outflows ($< 500 \text{ pc}$ Bertoldi et al. 1999; Neufeld et al. 2006a; Giannini et al. 2011; Yuan et al. 2012), photo dissociation regions (Wright et al. 1999), supernova remnants ($< 2 \text{ kpc}$ Yuan et al. 2012), or protoplanetary disks ($< 160 \text{ pc}$ Bergin et al. 2013; McClure et al. 2016). A very tentative detection of a single HD transition with ISO made towards Sgr B2 in the Galactic center was claimed by Polehampton et al. (2002), which will not be discussed further here.

The James Webb Space Telescope (JWST) now provides a unique opportunity to survey the [D/H] abundance throughout the Galaxy using MIRI/MRS to observe rotational lines of HD and H_2 with a single instrument. The sensitivity and spatial resolution of MIRI/MRS ($0.3\text{-}1.1''$) is greatly improved compared to previous mid-infrared facilities, allowing the H_2 and HD column densities and excitation conditions to be spatially mapped in great detail. Moreover, the MIRI/MRS range ($4.9\text{-}28.5 \mu\text{m}$) covers a variety of shock-tracing lines from iron and sulfur that are accessible in the mid-IR, allowing a comparison of [D/H] and the HD column densities across a variety of different shock environments and providing a potential means to test the dust depletion hypothesis. Finally, the greatly improved sensitivity of JWST allows the faint HD lines to be detected out to much larger distances in the Galaxy than possible before, potentially allowing the [D/H] abundance across the Galaxy to be better constrained.

In this paper, we report the detections of HD lines in 5 nearby bright protostellar outflows and 5 distant high mass protostars at Galactocentric radii (R_{GC}) from 4 to 11 kpc in the JWST Observations of Young protoStars (JOYS) program (Sect. 2). We compare the emission morphology and measure fluxes for H_2 , HD, and various lines tracing refractory elements in high-velocity jets ([Fe II], [S I]), use rotational diagrams to measure the H_2 and HD column densities or upper limits, and determine [D/H] abundance towards our sources in Sect. 3. In Sect. 4, we compare the observed line fluxes and properties of the H_2 and HD

Table 1. Sources analyzed for JWST MIRI/MRS H₂ and HD Observations

Source	d (pc)	R_{GC} (pc)	RA (J2000)	Dec (J2000)	Integration time (s) ¹	Pointings
High-mass						
IRAS 18089-1732	3600	4600	18:11:51.46	-17:31:28.8	600	2
G28 IRS 2	3700	4700	18:42:51.98	-03:59:54.0	600	1
G28 P1	3700	4700	18:42:50.70	-04:03:14.1	600	1
G31-A	3750	5200	18:47:34.32	-01:12:46.0	600	1
IRAS 23385+6053 (N)	4900	11000	23:40:54.48	+61:10:27.9	600	4
Low-mass						
L1448-mm	293	~ 8.0	03:25:38.76	+30:44:8.2	600	3
IRAS4B	293	~ 8.0	03:29:12.01	+31:13:7.1	600	2
BHR71-IRS1	199	~ 8.0	12:01:36.55	-65:08:53.6	600	9
Ser-emb-8N	436	~ 8.0	18:29:49.27	+01:16:52.6	600	1
HH 211	321	~ 8.0	03:43:58.10	+32:00:43.0	600	24

Notes. The distance relative to the solar system and the Galactocentric radius are denoted d and R_{GC} respectively.

The positions given are the pointing centers of the MIRI/MRS observations, which are generally offset from the protostar positions and centered on the blue outflow lobes ⁽¹⁾ Total integration time of all three gratings per pointing.

gas, and compare the [D/H] abundance between our sources and with Galactic chemical evolution models. We discuss the effects of the depletion of deuterium onto the dust grains, the possible variations in [D/H] across the Galaxy in the context of the Galactic chemical evolution models, and the outlook for future JWST studies of HD in Sect. 5. A summary and conclusions are provided in Sect. 6

2. Observations

Our MIRI/MRS data are from the JOYS programs 1290 (PI: E. F. van Dishoeck) and 1257 (PI: T. Ray), which target embedded protostars with the pointings generally centered on the continuum position or blue-shifted outflow lobes. Here, we included observations of 5 high-mass star-forming regions, and 5 nearby and bright low-mass sources where the outflows are well resolved. The details of the observations for each source are listed in Table 1. We select low-mass targets with multiple pointings which are bright in H₂ so that non-detections of HD can provide significant upper limits on [D/H], and all high-mass targets so that a wide range of Galactocentric radii are sampled, including IRAS 23385+6053 at 11 kpc and several targets in the inner Galaxy at ~ 4 kpc. We exclude the high-mass source G28-S, as no continuum source is detected even up to the longest MRS wavelength (28 μ m).

The data reduction details for HH 211 are described in Caratti o Garatti et al. (2024). For all other sources in program 1290, the reduction details are as follows. The data were taken using the FASTR1 readout mode and a two-point dither pattern in the negative direction which was optimized for extended sources. All three gratings (A, B, C) were used, covering the full 4.9–28.5 μ m wavelength range of MIRI-MRS. The number of pointings varies depending on the angular extent of the source and is listed in Table 1. Dedicated background observations were taken for all sources except G28 IRS 2 and G28 P1 to allow for a subtraction of the telescope background and detector artifacts. However, for IRAS 23385+6053, the background was not subtracted using the dedicated background since it also contains real astronomical continuum emission and PAH features (for details, see Beuther et al. 2023). Since the focus of this paper is

on emission lines, the subtraction of telescope background does not significantly alter the results. An astrometric correction was performed for IRAS 23385+6053 using GAIA DR3 stars in the parallel imaged field (Beuther et al. 2023).

The data were processed through all three stages of the JWST calibration pipeline (Bushouse et al. 2024) using reference context `jwst_1210.pmap` of the JWST Calibration Reference Data System (CRDS; Greenfield & Miller 2016). Both the science and background data were first processed through the `Detector1Pipeline` using the default parameters. Next, the data were further processed through `Spec2Pipeline`, which included the subtraction of the dedicated backgrounds for G31 and IRAS 18089-1732 as well as applying the fringe flat for extended sources (Crouzet et al. in prep.) and the residual fringe correction on the detector level (Kavanagh et al. in prep.). A bad-pixel routine was applied to the resulting `cal` files using the `Vortex Imaging Processing (VIP)` package (Christiaens et al. 2023). Lastly, the final data cubes were constructed for each subband of each channel individually using the `Spec3Pipeline`. In this final step, the master background and outlier rejection steps were switched off.

3. Analysis

3.1. Integrated line intensity maps

Spatially extended emission from many H₂, HD, and atomic lines is detected towards all of our sources (Table A.1 in App. A). The detected HD lines include transitions with much higher excitation energies than probed by previous mid- and far-IR observations, and range from R(4) ($E_{up} = 1895$ K) as high as the R(9) transition ($E_{up} = 6656$ K). To compare the morphology of the line emission, it is useful to inspect maps of the continuum subtracted and wavelength integrated line intensity. However, the MIRI/MRS point-spread-function (PSF) size varies significantly across the full wavelength range (0.3–1.1"), complicating the comparison. Furthermore, individual spaxels in the reconstructed MIRI/MRS data cubes can show amplitude rippling along the spectral axis from undersampling of the PSF at short wavelengths and residual fringing not removed by the pipeline. To enable an even comparison of the line intensities and mitigate

these artefacts, we perform a Gaussian convolution of each data cube to a resolution of $1''$, which is approximately the spatial resolution of MIRI/MRS at the wavelength of the longest analyzed line, [S I] at $25.25 \mu\text{m}$.

We estimate the continuum emission underlying each emission line by taking the median intensity over the wavelength axis in a 1000 km s^{-1} wide range centered around the line's rest wavelength. For each line, we then subtract the estimated continuum and integrate over the wavelength axis in a 400 km s^{-1} wide range centered on the line. This integration range is chosen to capture the full extent of the line because the velocity resolution of MIRI/MRS is only $\sim 100\text{--}200 \text{ km s}^{-1}$.

We show integrated line intensity maps of selected H_2 , HD, and atomic lines for IRAS 23385+6053 and HH 211 for selected lines in Figs. 1 and 2, the remaining maps and sources are shown in Figs. C.1 to C.8. Where present, emission from HD is seen to be brightest towards bright shocks where the high-J H_2 lines are detected.

In HH211, the locations where the HD emission peaks are strongly correlated with the [S I] and [Fe II] atomic lines tracing the high velocity inner jet and bow shock. Emission from [Fe I] is also bright in the inner jet where HD emission is detected, but not in the bow shock, likely reflecting differences in the ionization fraction of Fe. Similar correlations between the HD and atomic line emission are seen for the other nearby low-mass outflows, and for the high mass protostellar system IRAS 23385+6053 where multiple large scale outflows are being driven by embedded protostars, though over far larger scales of 1000s rather than 100s of au (Beuther et al. 2023; Gieser et al. 2023). HD emission is not clearly detected in the integrated line intensity maps in any other high-mass sources of the JOYS sample despite the similar sensitivities and distances.

3.2. Aperture spectral extraction

To quantitatively compare the line fluxes between different sources and outflow regions, we extract spectra from the convolved cubes described in Sect. 3.1. From inspection of the integrated line intensity maps in the low-mass sources, the HD lines appear brightest in the outflow jet knots and bow shock, but there are also many outflow locations with bright H_2 emission in the lower energy S(1) to S(3) lines ($E_{\text{up}} \sim 1000\text{--}2500 \text{ K}$) where the HD emission is faint despite a large column density of H_2 likely being present. To probe the origin of the HD, we thus extract spectra towards positions representative of the HD-bright jets and bow-shocks, as well as the fainter positions in the outflow cavities. For the nearby low-mass sources, we extract multiple apertures to compare conditions across the outflows, while we use only a single aperture for each high-mass source owing to their much greater distance. The locations and sizes of our extracted apertures are shown as green circles overlaid on the line intensity maps described in Sect. 3.1 and App. C, and we list their positions in Table B.1 of App. B.

For each position, we extract a spectrum by taking the sum of the flux in a $1''$ radius aperture. As all data cubes have been convolved to the same resolution of $1''$, the aperture radius is kept constant with wavelength. We then apply a residual fringe correction to the 1D spectrum (Kavanagh et. al. in prep). To measure the flux of the H_2 , HD, and selected atomic lines, we fit each line with Gaussian profile and a first-order polynomial to represent the continuum. When a line is not detected, we take as an upper limit on the flux $F_{\text{up}} = 3\sigma_{\text{RMS}}\text{FWHM}$, where σ_{RMS} is measured in a small line-free region adjacent to the expected line, and FWHM is the full width at half-maximum of MIRI/MRS spec-

tral response. This empirical approach in determining the upper limits incorporates both the sensitivity limits of MIRI/MRS and calibration uncertainties, e.g. residual high-frequency fringing remaining in the spectrum.

We show line detections and Gaussian fits for two representative apertures from HH 211 and IRAS 23385+6053 in Figs. 3 and D.1, respectively. The fluxes for all lines and apertures are reported in Tables E.1 to E.3 in App. E. The lines are generally unblended, except for the HD R(6) line which can overlap with a bright transition of H_2O in some cases, and the HD R(7) line which can become partially blended with CO_2 Q and P-branch transitions. Bright OH transitions are often detected close to the HD R(6) line but do not overlap it.

3.3. Rotation diagram analysis

We use a rotation diagram analysis to measure the column density of H_2 and HD, and thus determine the [D/H] abundance or upper limits for our targets. Under the assumption that the line emission is optically thin and in local thermodynamic equilibrium (LTE), a rotation diagram provides a simple way to determine the column density and kinetic temperature of the gas (Mangum & Shirley 2015). The extinction-corrected line intensities I_{ul} (explained below) are used to compute the quantity for the y-axis of the diagram

$$y = \ln(N_u/g_u) = \ln\left(\frac{4\pi I_{ul}}{A_{ul}h\nu g_u}\right),$$

where N_u is the column density of molecules in the upper state of the transition, g_u the upper state degeneracy, A_{ul} the Einstein A emission coefficient, and $h\nu$ the photon energy. The x-axis of the diagram is the upper state energy $x = E_u/k$ in units of K, and on such a diagram a linear fit of the form $y = mx + b$ will yield the column density of the gas and temperature via: $m = -1/T$ and $b = \ln(N/Q(T))$, where N is the total column density of the molecule and $Q(T)$ is the partition function.

To convert the wavelength-integrated line fluxes from Sect. 3.2 to the intensity needed for the rotation diagrams, we assume that the H_2 or HD emission fills the aperture. This assumption should be reasonable for the nearby low-mass sources, as modeling of the H_2 excitation in shocks indicates that most should be spatially resolvable by JWST/MIRI for shock densities $\leq 10^6 \text{ cm}^{-3}$ (Kristensen et al. 2023, Figure 9). For the distant high-mass sources the emission solid angle may be much smaller than the aperture, but we nonetheless make the same assumption. In any case the assumed emission solid angle is the same for both H_2 and HD and thus there is no impact on any column density ratios or the derived [D/H]. The observed line intensity $I_{ul,\text{obs}}$ is then $I_{ul,\text{obs}} = F_{ul,\text{obs}}\Omega$, where $F_{ul,\text{obs}}$ is the sum of the integrated line flux in the extraction aperture with solid angle Ω equal to a circle with radius $1''$.

The extinction correction needed for the line intensities can be derived using the H_2 rotation diagrams and a wavelength dependent extinction law $A_\lambda(A_K)$. In Fig. F.1 of App. F, we show the KP5 (Pontoppidan et al. 2024) extinction curve at A_K values ranging from 1 to 10. This theoretical extinction curve constrained by observations is appropriate for dense molecular clouds, and contains absorption features from silicates and various ice species. It has been shown to perform well for extinction correction of H_2 lines in JWST spectra (Narang et al. 2024). The $J = 1 - 4$ transitions are particularly useful as a measure of extinction, as the S(3) transition at $\sim 9.66 \mu\text{m}$ is found within the broad $10 \mu\text{m}$ silicate feature, whereas the S(1), S(2), and S(4)

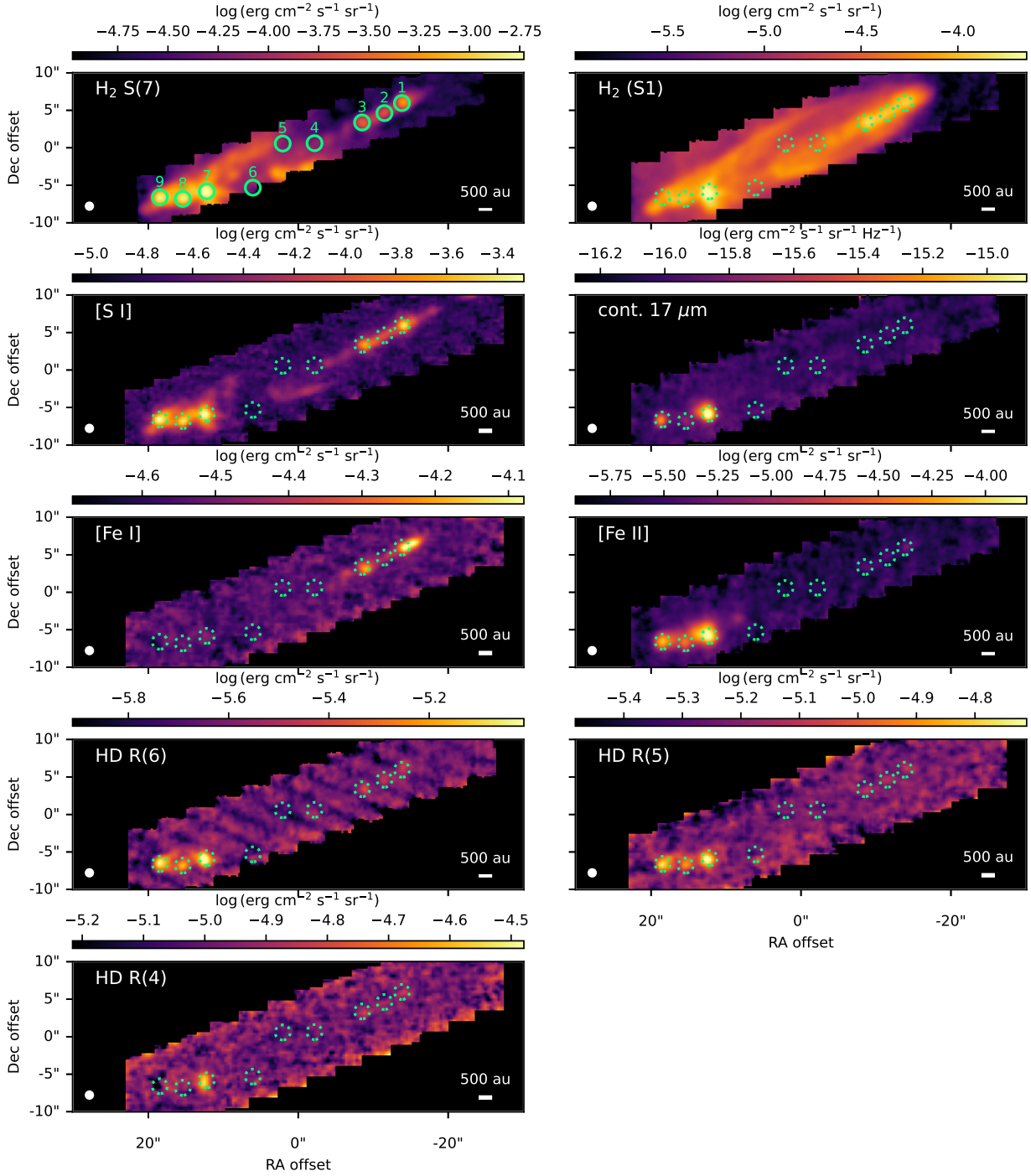


Fig. 1. Integrated line intensity maps for HH 211 of various lines and the continuum at $17\ \mu\text{m}$ shown with a logarithmic stretch. The maps have been smoothed to a common resolution of $1''$, shown by the white circle in the bottom-left. Apertures used for spectral extraction are shown by the green circles. An index for each aperture is provided in the top-left panel. The coordinates of the aperture centers can be found in Table B.1 of App. B.

transitions lie outside this feature and experience approximately the same extinction. Using the uncorrected intensities to produce a rotation diagram, the S(3) transition will thus appear relatively suppressed, as has been found in many previous H_2 studies (e.g. Bertoldi et al. 1999; Neufeld et al. 1998). By fitting a single temperature component with a variable A_K to the S(1) to S(4) transitions, the rotation diagram is effectively linearized. Specifically, a fit to the rotation diagram using the uncorrected intensities is

done with the relation:

$$y_{\text{obs}} = \ln \left(N_{\text{warm}} \frac{\exp(-x/T_{\text{warm}})}{Q(T_{\text{warm}})} 10^{-A_{\lambda}/2.5} \right),$$

where

$$y_{\text{obs}} = \ln \left(\frac{4\pi I_{ul,\text{obs}}}{A_{ul} h\nu g_u} \right).$$

We perform this fit with equal weighting on all lines because of the importance of the relatively faint S(3) line in the determi-

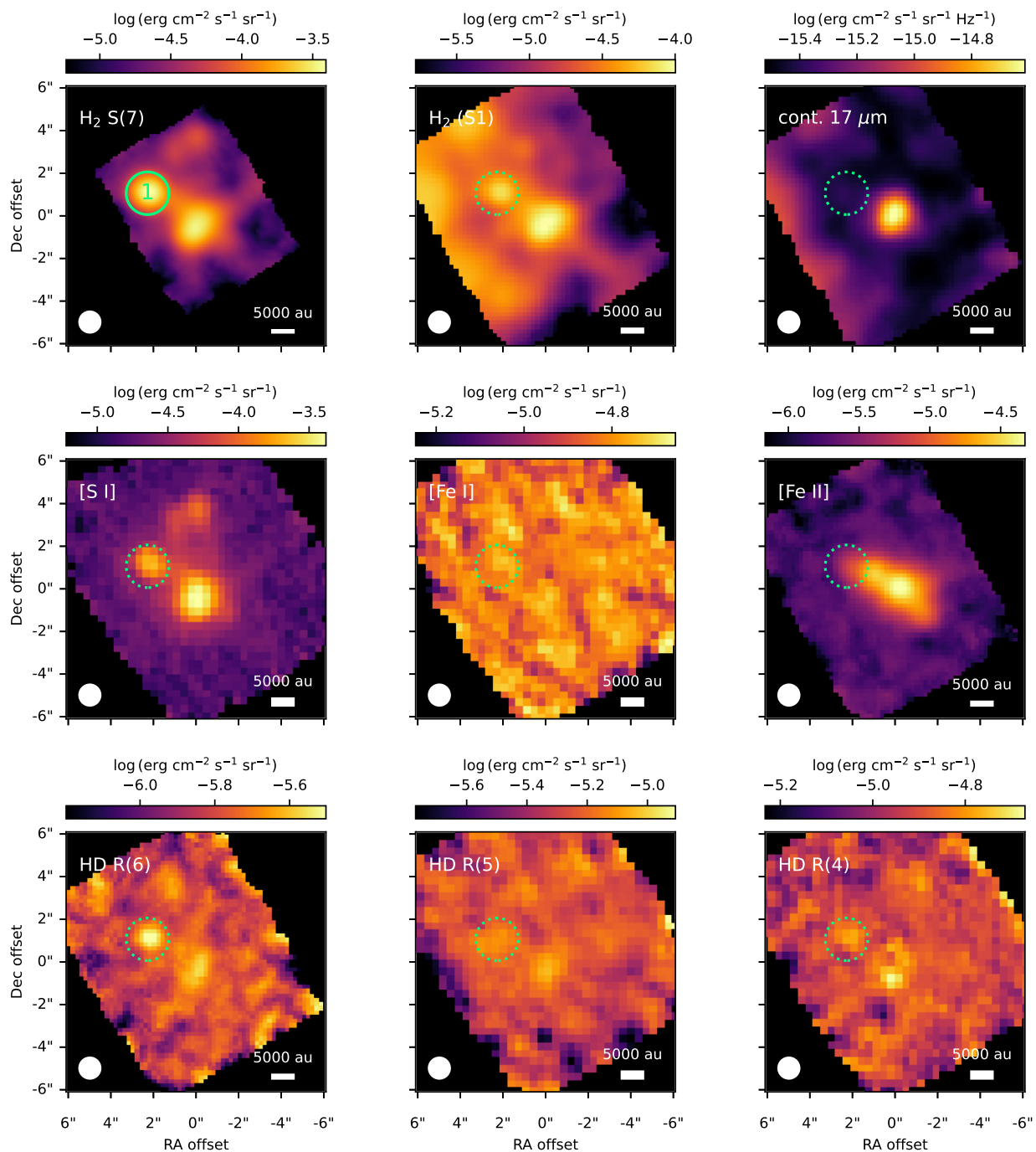


Fig. 2. Same as Fig. 1, but for IRAS 23385+6053.

nation of the extinction. We show the effects of this correction for HH 211 and IRAS 23385+6053 in Fig. F.2 in App. F.

After correction for extinction, our H_2 rotation diagrams all show some amount of curvature in the higher upper energy S(5)-S(8) lines and are thus not well described by a single temperature component. Optically thick emission can produce curvature in a rotation diagram, but this should not be significant for H_2 or HD rotational emission in protostellar outflows given the low column density of the gas and small Einstein coefficients. A more reasonable explanation is the presence of multiple temperature components in different shock environments in the aperture. This also produces curvature in a rotation diagram, and has

been noted in many previous studies of H_2 emission from outflows (van Dishoeck 2004; Yuan & Neufeld 2011; Yuan et al. 2012). In addition to curvature, some of our H_2 rotation diagrams show a zigzag pattern where the ortho (odd- J) transitions are suppressed relative to the para (even- J) transitions (See Fig. F.3). This is characteristic of an ortho-to-para H_2 column density ratio less than the typical value of 3 reached in local thermodynamic equilibrium (Neufeld et al. 2006b).

To fit the extinction corrected H_2 rotation diagrams, we thus use a two-temperature model with an additional correction for

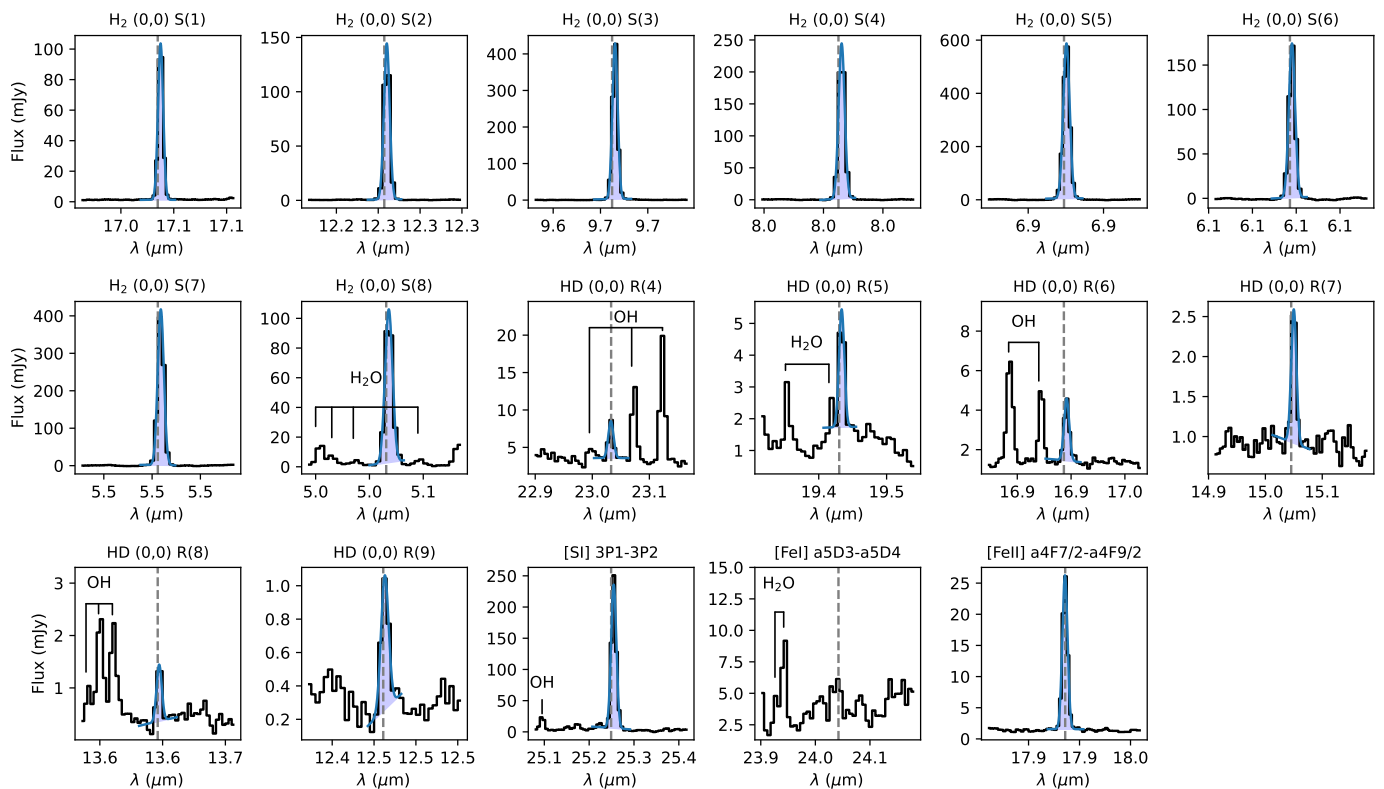


Fig. 3. Spectral line fits for H₂ (top two rows), HD (rows 3 and 4), and the [S I], [Fe I], and [Fe II] atomic lines (rows 4 and 5) for HH 211 aperture 8. The line flux (shaded blue region) is determined by the simultaneous fit of a Gaussian profile and a first order polynomial to represent the continuum. The rest-frame wavelength of each spectral line is shown by a dashed grey line, and non-detections are shown without a shaded region for the fit. Nearby molecular lines of are labelled.

the ortho-to-para correction term:

$$y = \ln \left(N_{\text{warm}} \frac{\exp(-x/T_{\text{warm}})}{Q(T_{\text{warm}})} + N_{\text{hot}} \frac{\exp(-x/T_{\text{hot}})}{Q(T_{\text{hot}})} \right) + z(J),$$

where $N_{\text{tot}} = N_{\text{warm}} + N_{\text{hot}}$, for a warm component ($T_{\text{warm}} = 250 - 1000$ K) and hot component ($T_{\text{hot}} = 1000 - 6000$ K), and where

$$z(J) = \begin{cases} \ln \left(\frac{\text{OPR}}{3} \right) & \text{odd } J \\ 0, & \text{even } J \end{cases},$$

and OPR is the ortho-to-para ratio. Representative fits for IRAS 23385+6053 and HH 211 are shown in the top row of Fig. 4. We summarize the H₂ fit results in Table G.1. We note that the error bars on the fit parameters include only the uncertainty propagated from the line flux measurements; we consider the effect of uncertainty in A_K on deriving [D/H] in Sect. 3.4.

The majority of our H₂ rotation diagrams are well described by two temperature components in LTE with OPR = 3. In some cases, OPR = 2 – 3 is found, but the values of the warm and hot components are still consistent with LTE. For a handful of positions associated with very bright bow-shocks, the rotation diagrams become nearly horizontal for the higher excitation transitions (S(4) to S(8)). Here, the temperature of the hot component is very poorly constrained and reaches the maximum allowed in the fit of 3000 K. This suggests a still hotter component of the H₂ emission, which has been detected in rovibrational emission from other outflows with ISO-SWS and JWST/NIRSpec (van Dishoeck et al. 1998; Giannini et al. 2008, 2015; Le Gouellec et al. 2024). In any case, the column density of the warm H₂ component which we use in our estimate of [D/H] is determined

almost entirely by the S(1) to S(4) lines, for which the temperature is well constrained.

The rotation diagram fits for HD are somewhat simpler, as we see little evidence of multiple temperature components, and HD does not have ortho and para forms. Since the HD is also only present in the outflow, it should experience the same extinction as H₂, and we thus correct the line intensities using the same value for A_K , and perform a fit of a single temperature component to the rotation diagram. Representative fits for IRAS 23385+6053 and HH 211 are shown in the bottom row of Fig. 4. We note that the excitation energies of the HD R(4) to R(6) lines are similar to the H₂ S(2) to S(4), so the single component fit to the HD transitions should trace gas with similar excitation conditions as the warm component in the H₂ fits, which dominates N_{tot} . However, the much larger Einstein coefficients of the HD transitions than those of H₂ result in a higher critical density, and deviations from LTE may become significant for the low densities in protostellar outflows. We discuss this further in Sect. 3.4, where we correct for non-LTE conditions in our determination of [D/H]. We note that we do not consider a temperature gradient as in previous works analyzing Spitzer detections of HD (Yuan & Neufeld 2011; Yuan et al. 2012), as the HD lines analyzed here are not sensitive to the cold (< 300 K) gas that could be probed with the lower excitation HD lines detectable with Spitzer.

For our other JOYS targets where H₂ is detected but no HD lines are observed, we can estimate upper limits on the HD column density. We convert each HD line upper limit to a column density assuming the temperature of the warm component of H₂ in the rotation diagram fits, and applying the same extinction correction to the line intensities as was derived for H₂. We take

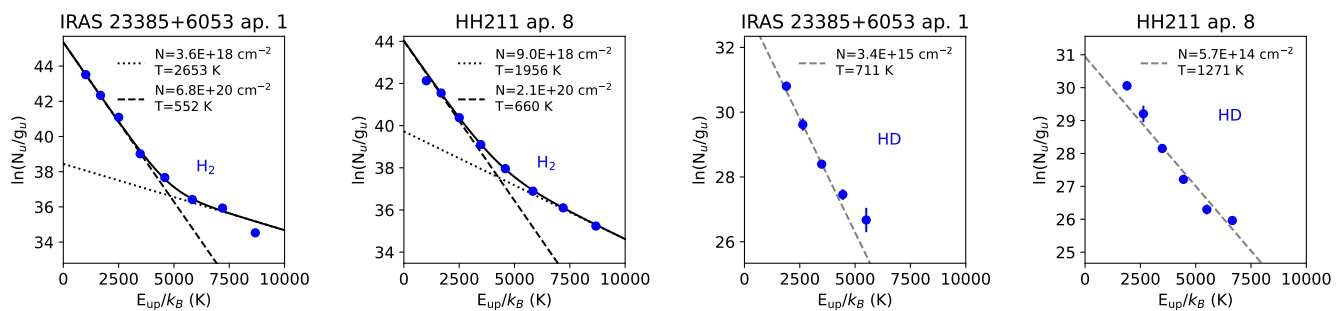


Fig. 4. Rotational diagrams for the detected H_2 (top row) and HD (bottom row) transitions in IRAS 23385+6053 aperture 1 and HH 211 aperture 8. Corrections for extinction and an ortho-to-para ratio < 3 have been applied (see text and App. F).

the lowest column density upper limit of the three transitions as our overall 3σ upper limit for each observation. We note that despite the much lower sensitivity in channel 4 of MIRI/MRS, the most constraining upper limit is typically from the $23.04 \mu\text{m}$ R(4) line of HD, as this transition lies at the lowest upper energy level (see Table A.1). We summarize the results of our HD rotation diagram fits in Table G.1. Where we have detections of HD, 3-5 transitions are detected, which provides much more precise constraints on the column density and temperature of HD in protostellar outflows than possible with previous facilities. In general, we find the excitation temperatures of the single component for HD to be intermediate between the temperatures of the warm and hot H_2 components, typically 500-1000 K, and the column density of HD to be ~ 5 orders of magnitude lower than that of the warm H_2 component. We can thus rule out that enhancement of HD by orders of magnitude relative to H_2 is occurring, as is often the case for other complex deuterated species (Ceccarelli et al. 2014).

3.4. $[\text{D}/\text{H}]$ abundance and upper limits

As a starting point to determine $[\text{D}/\text{H}]$ abundances, we can assume LTE holds, and compare the column density from the warm component of H_2 with that of HD traced the same approximate ranges in upper energy of the transitions. For our protostellar outflows, we assume that the outflows are almost entirely molecular H_2 , except for a core of atomic H associated with the jet, as has been found for HH 211 (Caratti o Garatti et al. 2024). The $[\text{D}/\text{H}]$ abundance or upper limit is then simply $[\text{D}/\text{H}] = \frac{1}{2} N_{\text{HD}}/N_{\text{H}_2}$. However, at densities $< 1 \times 10^6 \text{ cm}^{-3}$ that can occur in protostellar outflows, non-LTE deviations in the level populations for the $J > 4$ HD lines are significant (Bertoldi et al. 1999). Prior estimates of the H_2 from a non-LTE analysis of a handful of detected HD transitions towards the L1448 outflow suggest that densities $< 1 \times 10^6 \text{ cm}^{-3}$ are indeed present in some regions of the flow (Giannini et al. 2011). Bertoldi et al. (1999) show that not accounting for the non-LTE excitation can result in an overestimate of the HD column density. For their analysis of HD in the Orion OMC-1 outflow, they found that non-LTE excitation increases the inferred column density by a factor of ~ 1.47 relative to an LTE model, though the exact correction factor is sensitive to the shock density, temperature, and dissociation fraction.

Another important effect on the derived deuterium abundance considered by Bertoldi et al. (1999) is the chemical conversion of HD to D via: $\text{HD} + \text{H} + \Delta H_0 \rightleftharpoons \text{D} + \text{H}_2$, where $\Delta H_0 = 418 \text{ K}$ is the enthalpy difference. This can be significant in the warmest and densest parts of C-type shocks present

in some regions of protostellar outflows, though HD reforms in the cooler post-shock regions. For the Orion OMC-1 outflow, Bertoldi et al. (1999) found that the average effect over the entire shock region was to reduce the HD abundance relative to H_2 by a factor of 1.67. When the effect of chemical conversion is combined with the non-LTE excitation, their true $[\text{D}/\text{H}]$ abundance is a factor of 2.45 higher than what would be inferred from a purely LTE analysis. Interestingly, Bertoldi et al. (1999) find that this result is not particularly sensitive to how dissociative the shock is. In a less dissociative shock with a smaller fraction of atomic H, chemical conversion of HD to D is weaker but the correction for non-LTE effects is larger, and the combined correction factor is approximately constant. To account for the combined effects of chemical conversion and non-LTE excitation of HD, we thus follow Bertoldi et al. (1999) and multiply our LTE $[\text{D}/\text{H}]$ estimates by a factor of 2.45.

An estimate for the uncertainty for $[\text{D}/\text{H}]$ should also include the effect of extinction. However, the uncertainty in the column densities of warm H_2 and HD from Sect. 3.3 includes only the propagated errors on the line fluxes, as A_K was held fixed to the value determined from the S(1) to S(4) transitions of H_2 . To estimate the effect of A_K uncertainty on the derived $[\text{D}/\text{H}]$, we rerun our two component fits with A_K up to two magnitudes larger or smaller than the best fit value. As an example, we show this procedure for IRAS 23385+6053 in Fig. F.4 in App. F. The resulting column densities for warm H_2 and HD are shown as a function of A_K in the upper panel, while the derived $[\text{D}/\text{H}]$ is shown in the lower panel. Since both the HD and H_2 column densities are strongly correlated with any change in A_K , the overall effect on $[\text{D}/\text{H}]$ is small. We take as our uncertainty in A_K the result from the fit of a single temperature component to the S(1) to S(4) transition (green shaded region in lower panel of Fig. F.4), and convert this to an uncertainty in $[\text{D}/\text{H}]$ (blue shaded region in lower panel of Fig. F.4). We include the uncertainty of A_K in our final estimate of $[\text{D}/\text{H}]$ by adding it in quadrature with the uncertainty propagated from the fits to the rotation diagrams.

4. Results

We summarize our inferred deuterium abundances or upper limits in Table 2, and also list the Galactocentric radius R_{GC} to each source. For apertures and sources with a non-detection of HD and low column densities and/or low temperatures of the warm H_2 component, the upper limits on the HD column density result are low as the HD lines are not expected to be bright. This results in corresponding upper limits on $[\text{D}/\text{H}]$ which are well above the primordial abundance of $2.58 \pm 0.13 \times 10^{-5}$ (Cyburt et al. 2016), and thus not constraining.

Table 2. [D/H] Abundances from mid-IR rotational lines

Source + Aperture	R_{GC}	[D/H] $\times 10^{-5}$	ref.
G28-IRS2 ap. 1	4.7	< 4.81	JOYS
G28-P1-A ap. 1	4.7	< 1.90	JOYS
G31-A ap. 1	5.2	< 3.69	JOYS
IRAS 18089-1732 ap. 1	4.6	< 0.71	JOYS
IRAS 23385+6053 ap. 1	11.0	0.61 ± 0.30	JOYS
BHR71-IRS1 ap. 1	~ 8.0	1.90 ± 1.03	JOYS
BHR71-IRS1 ap. 2	~ 8.0	1.06 ± 0.46	JOYS
BHR71-IRS1 ap. 3	~ 8.0	1.26 ± 0.25	JOYS
BHR71-IRS1 ap. 4	~ 8.0	< 2.46	JOYS
HH 211 ap. 1	~ 8.0	1.30 ± 0.49	JOYS
HH 211 ap. 2	~ 8.0	1.74 ± 0.14	JOYS
HH 211 ap. 3	~ 8.0	1.78 ± 0.47	JOYS
HH 211 ap. 4	~ 8.0	< 1.17	JOYS
HH 211 ap. 5	~ 8.0	< 0.86	JOYS
HH 211 ap. 6	~ 8.0	< 2.92	JOYS
HH 211 ap. 7	~ 8.0	0.25 ± 0.18	JOYS
HH 211 ap. 8	~ 8.0	0.33 ± 0.15	JOYS
HH 211 ap. 9	~ 8.0	0.44 ± 0.34	JOYS
IRAS 4B ap. 1	~ 8.0	0.12 ± 0.07	JOYS
IRAS 4B ap. 2	~ 8.0	0.12 ± 0.06	JOYS
L1448-mm ap. 1	~ 8.0	1.66 ± 0.42	JOYS
L1448-mm ap. 2	~ 8.0	2.27 ± 0.21	JOYS
L1448-mm ap. 3	~ 8.0	2.24 ± 0.36	JOYS
L1448-mm ap. 4	~ 8.0	< 1.38	JOYS
Ser-emb 8 (N) ap. 1	~ 8.0	0.92 ± 0.45	JOYS
Ser-emb 8 (N) ap. 2	~ 8.0	0.57 ± 0.38	JOYS
Local disk [D I]/[H I]	~ 8.0	2.00 ± 0.10	^a
Local disk [D I]/[O I]	~ 8.0	0.70 ± 0.20	^b
Orion Bar	8.4	1.00 ± 0.30	^c
Orion OMC	8.4	0.76 ± 0.29	^d

All listed JOYS values have been corrected upwards for chemical conversion of HD by a factor of 2.54 (see text).

^a (Prodanović et al. 2010).

^b (Hébrard 2010).

^c (Wright et al. 1999).

^d (Bertoldi et al. 1999).

We also include in Table 2 literature [D/H] measurements that have been derived from rotational lines of HD and H₂ observed in a protostellar outflow and photodissociation region (PDR) with ISO (Bertoldi et al. 1999; Wright et al. 1999). We note that similar rotation-line-based [D/H] measurements are available from *Spitzer* observations of two nearby protostellar outflows and a supernova remnant (Yuan et al. 2012), however, the Yuan et al. (2012) [D/H] values have systematic uncertainties of a factor of a few depending on whether spectroscopic or imaging data is used to estimate line fluxes, and thus are not particularly constraining. A detection of DCN in a cloud ~ 0.1 pc from the Galactic center was reported by Lubowich et al. (2000), and through comparison with an HCN line and chemical fractionation modelling [D/H] = $1.7 \pm 0.3 \times 10^{-6}$ was claimed, however, this result may also vary by an order of magnitude or more given the systematic uncertainty associated with fractionation models and their strong temperature dependence. Finally, we also include the [D/H] = $2.0 \pm 0.1 \times 10^{-5}$ in the local Galactic disk derived through UV absorption lines of D I and H I (Prodanović et al. 2010), and the [D/H] = $7.0 \pm 2.0 \times 10^{-6}$ derived from D I and O I lines and scaling by the ISM oxygen abundance (Hébrard 2010).

Fig. 5 presents our sources with detected HD lines and a [D/H] measurement (including the upwards correction factor of 2.45 for non-LTE effects and chemical conversion, see Sect. 3.4), or a [D/H] upper limit below the primordial abundance. Significant variations in [D/H] abundance of a factor ~ 4 are seen between detected sources. The outflows from low-mass protostars (green symbols in Fig. 5) originate from star-forming regions at similar positions in the Galactic disk. These regions should have formed from gas that has experienced similar levels of astration and thus with nearly the same [D/H] abundance (discussed further in Sect. 5). This should certainly be true when comparing different positions from the same outflow (e.g. HH 211 and L1448-mm), however, a similar magnitude of variation as between different sources is seen instead. We note that in HH 211 [D/H] is robustly lower in the bow-shock positions (apertures 1-3) than the jet positions (apertures 4-6), hinting at a link between the shock environment and [D/H]. Overall, it is thus unlikely that the [D/H] variations seen are the result of differences in the degree of astration for the low-mass sources. However, it is crucial to note that the [D/H] derived from observations, whether from rotational H₂ and HD lines or H I and D I absorption lines, is only sensitive to the gas-phase component. Galactic chemical evolution (GCE) models make predictions for the total [D/H], including both molecular and atomic forms and any deuterium sequestered in dust grains or deuterated PAHs.

We note that the factor of ~ 4 abundance variation is similar to that seen by Linsky et al. (2006) and Prodanović et al. (2010) when comparing their UV absorption [D/H] measurements along different sight lines in the local Galactic disk, which they attribute to variations in the degree of deuterium depletion onto dust grains. It is thus plausible that the same depletion effect could explain the variations we see between different outflows and outflow positions, which we investigate further in the following Section.

4.1. Line flux and rotation diagram correlations

As noted in Sect. 3.1, the integrated line intensity maps show that the morphology of the HD emission is clearly associated with the jets and bow-shocks in our sources. The HD emission is particularly bright towards outflow positions that are also bright in [Fe I] and [S I]. Iron and Sulfur are both known to be depleted onto dust grains (Jenkins 2009), though the exact reservoir of the latter is not well-understood (Anderson et al. 2013; Kama et al. 2019). A possible explanation for the association between HD, [Fe I], and [S I] is that deuterium is significantly depleted onto dust grains, and is subsequently released along with Fe and S in strong shocks where the dust grains are destroyed. Free atomic D can be readily converted to HD via $D + H_2 \rightarrow HD + H$.

To perform a more quantitative comparison, we can investigate correlations between the extracted line fluxes and the rotation diagram fit parameters in all of our apertures. We first apply the same extinction correction derived from the H₂ rotation diagrams to all of our line fluxes using the method described in Sect. 3.3. We note that since the emission is extended and should fill the extracted apertures, the line flux and intensity are different only by a constant factor of the aperture solid angle. We show in the top row of Fig. 6 correlations between the HD R(6) line and 3 other lines associated with the outflow jets or bow-shocks: [S I], [Fe I], [Fe II]. A particularly strong correlation ($\rho = 0.95$) is seen between the HD R(6) line and [S I], while the correlation with [Fe I] and [Fe II] exhibit much more scatter ($\rho = 0.36$ and $\rho = 0.57$ respectively). This is possibly due to variations in the ionization conditions between different shocks that affect

the intensity of the [Fe I] and [Fe II] lines, but which are not as significant for [S I]. Namely, the ionization potential of the [Fe I] line is only 7.9 eV while for [S I] it is 10.36 eV. In the bottom row of Fig. 6, we show correlations between the HD R(6) line and the H₂ S(1), S(4), and S(7) lines. Strong correlations are seen particularly with the higher upper-energy S(7) line ($E_{\text{up}} \sim 7200$ K), suggesting the HD R(6) emission is associated with the denser and higher temperature components of the outflow.

While the association of the HD emission with dense and shocked regions of the outflows is clear, stronger evidence of D depletion and release in shocks would be a correlation between [D/H] and the gas phase abundance of refractory species or some measure of the degree of dust grain destruction. Determining the degree of dust destruction in the outflow shocks is non-trivial, however. For the case of HH211, modeling of the gas-phase abundance of Fe towards bright H₂ knots in the inner jet and bow shock has been performed by Caratti o Garatti et al. (2024) using the models of Hollenbach & McKee (1989). Their results show that the gas-phase iron abundance in all shock knots are depleted with respect to the solar value, and the knots in the inner jet are less depleted than those in the bow shock. (Caratti o Garatti et al. 2015, Fig. 13). This is the opposite of the expectation that the gas-phase iron abundance should be higher further along the flow as more grain destruction occurs and more Fe is released (Nisini et al. 2005; Podio et al. 2006). However, it is consistent with the increased [D/H] in the inner jet (apertures 4-6) relative to the bow-shocks in HH 211 (apertures 1-3), suggesting depletion of deuterium into dust grains is indeed a plausible mechanism. We note that two important caveats in the

modeling of Caratti o Garatti et al. (2024) are the uncertainty in the shock velocity and density, which makes the relative Fe depletion somewhat uncertain, and the assumption that sulfur is undepleted in the line ratios used, which affects the absolute gas-phase abundance. To confirm the link between dust depletion and [D/H] variations in the outflow, further modeling of the shock conditions and degree of refractory depletion is needed.

4.2. [D/H] variations and Galactic chemical evolution

Galactic chemical evolution models make predictions for the total [D/H] abundance throughout the Galactic disk that can in principle be compared with observations. This is useful for both placing constraints on the GCE models themselves and assessing the potential effects of deuterium depletion on the observed [D/H]. We thus plot in Fig. 7 as a function of R_{GC} the average [D/H] of our low-mass sources, the [D/H] measurement or upper limits for our high-mass sources, [D/H] from previous ISO measurements, and [D/H] measurements based on UV absorption lines. We overlay the primordial deuterium abundance of Cyburt et al. (2016), as well as total [D/H] gradients from GCE models selected from Romano et al. (2006) and van de Voort et al. (2018).

If we interpret our [D/H] measurements derived from HD and H₂ as representative of total [D/H], their values are generally much more similar to the low estimates of the local disk [D/H] of Hébrard & Moos (2003) and Hébrard (2010) than the high estimates of Linsky et al. (2006) and Prodanović et al. (2010). As noted in Sect. 1, the debate on which value represents the present

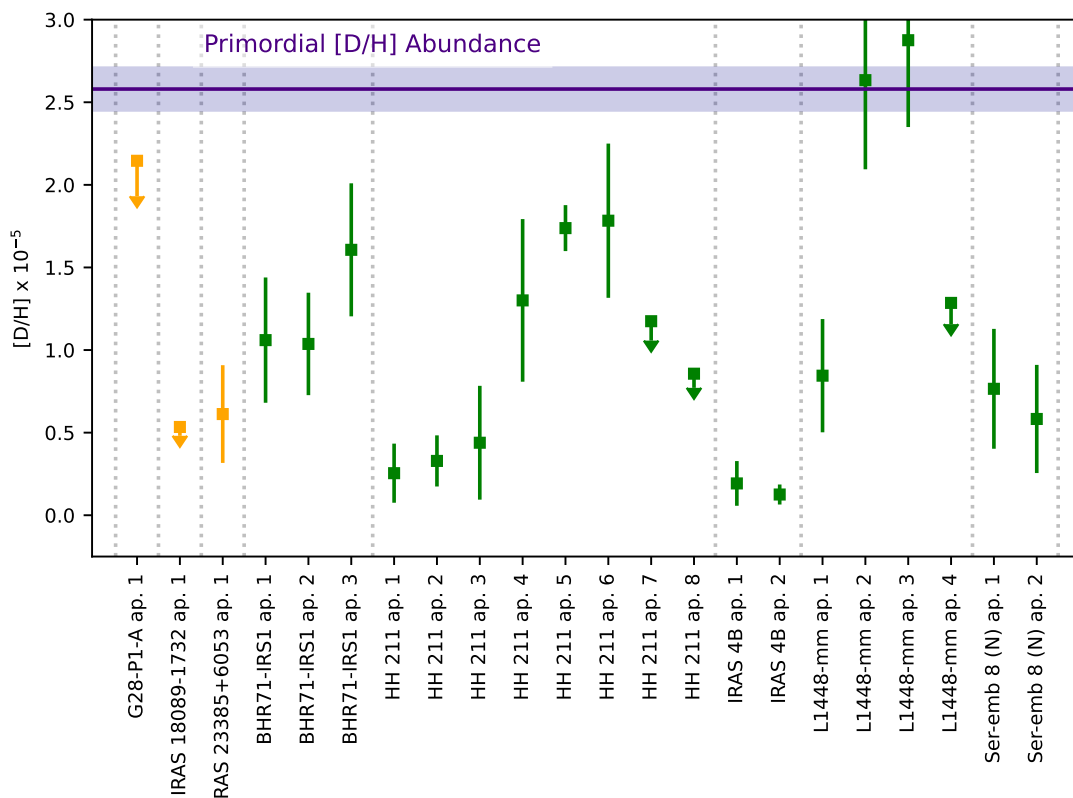


Fig. 5. Comparison of [D/H] abundance (Table 2) in this work. A correction factor of 2.54 has been applied to our [D/H] measurements (see text). Orange symbols show [D/H] in apertures for high-mass sources, while green symbols show [D/H] in apertures from low-mass sources. The dotted grey lines separate different sources. The blue shaded region shows the primordial total [D/H] abundance of (Cyburt et al. 2016). [D/H] upper limits above the primordial abundance are omitted.

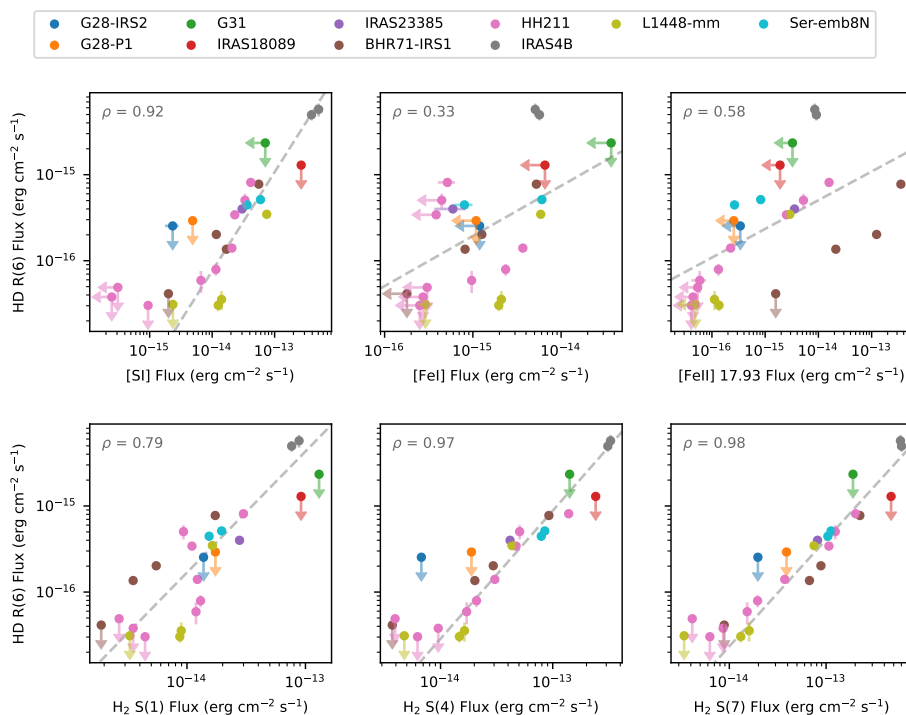


Fig. 6. Correlations between the extinction corrected flux of the HD R(6) line measured in all apertures for our sample with the extinction corrected flux of various atomic and H₂ lines. The line flux is related to the line intensity by a constant factor of the aperture solid angle (see text). *Top row:* Correlation with the [S I], [Fe I], and [Fe II] line flux. *Bottom row:* Correlation with the H₂ S(1), S(4), and S(7) line flux.

Galactic disk [D/H] abundance within a few kpc of the Sun remains unsettled, and the significance of the inferred depletion onto dust grains and the uncertainties in abundances and GCE effects introduced by using [D/O] as a proxy are both debated (Tosi 2010). However, the molecular line measurements and the low local disk [D/H] are typically a factor of $\sim 2 - 4$ below the predictions of the GCE models. The model of Romano et al. (2006) is based on the GCE code of Chiappini et al. (2001), and simultaneously satisfies existing chemical abundance constraints while being marginally able to reproduce the depletion-corrected [D/H] of Prodanović et al. (2010). Romano et al. (2006) have explored whether GCE models can reproduce the low values of [D/H] in the local Galactic disk of $< 1.0 \times 10^{-5}$ from Hébrard (2010) by increasing the efficiency of star formation in the solar neighbourhood, and thus the amount of astration. However, the increased star formation also produces more enrichment of the local Galactic disk with metals, and a resulting metallicity distribution for G and K type stars in the solar neighbourhood with much larger [Fe/H] than is observed. Similar problems in fitting this metallicity distribution occur if the amount of infall onto the Galactic disk of deuterium-rich and metal-poor gas is instead decreased.

It is also interesting to compare the [D/H] predictions from GCE models which are not aimed at specifically reproducing the abundance constraints from our Galaxy. In the context of the evolution of the [D/H] abundance in galaxies with cosmic time, van de Voort et al. (2018) have performed GCE simulations based on cosmological zoom-in simulations for galaxies forming over a wide range of redshifts and metallicity. The selected model shown in Fig. 7 shows the total [D/H] gradient for a typical milky way-like galaxy. The high [D/H] across the disk is much more consistent with the local disk [D/H] of Prodanović et al. (2010) that includes a correction for dust depletion.

GCE models generally predict an increasing total [D/H] with galactocentric radius owing to the increased star formation, and thus astration towards the Galactic center. Our high-mass protostar targets with detections or constraining upper limits on [D/H] are located in the inner and outer Galaxy, and may therefore be useful for measuring this predicted gradient, with the caveat of possible dust depletion. We detect HD lines only in the the local low-mass protostars and in IRAS 23385+6053 at $R_{GC}=11$ kpc, but not in any of our inner Galaxy targets. Taken at face value, the upper limit for IRAS 18089-1732 in particular would be consistent with a [D/H] gradient, however, we can not rule out the possibility that deuterium is more depleted onto dust in the inner Galaxy than in the local disk or outer Galaxy.

5. Discussion

In summary, our results show large variations in [D/H] between our local low-mass sources, and the derived values of [D/H] are generally a factor of $\sim 2 - 4$ lower with respect to the predictions of Galactic chemical evolution models. Several of our low-mass sources also show a [D/H] at nearly the primordial value (Fig. 5). If depletion is the underlying cause for the variations in [D/H], this would suggest that the total [D/H] is underestimated in many of our objects when derived from the molecular lines alone. Variable dust depletion would resolve the tension with the various GCE models shown in Fig. 7, which are generally unable to produce a low [D/H] and satisfy other abundance constraints. However, we do not see any clear trends in [D/H] abundance in comparison with the fluxes of the [S I] and [Fe I] lines, which could trace refractory material in dust grains released in shocks. One possible reason is that deuterium is thought to be depleted by replacing H-C bonds in carbonaceous dust grains or deuterated PAHs, with the latter experiencing different shock condi-

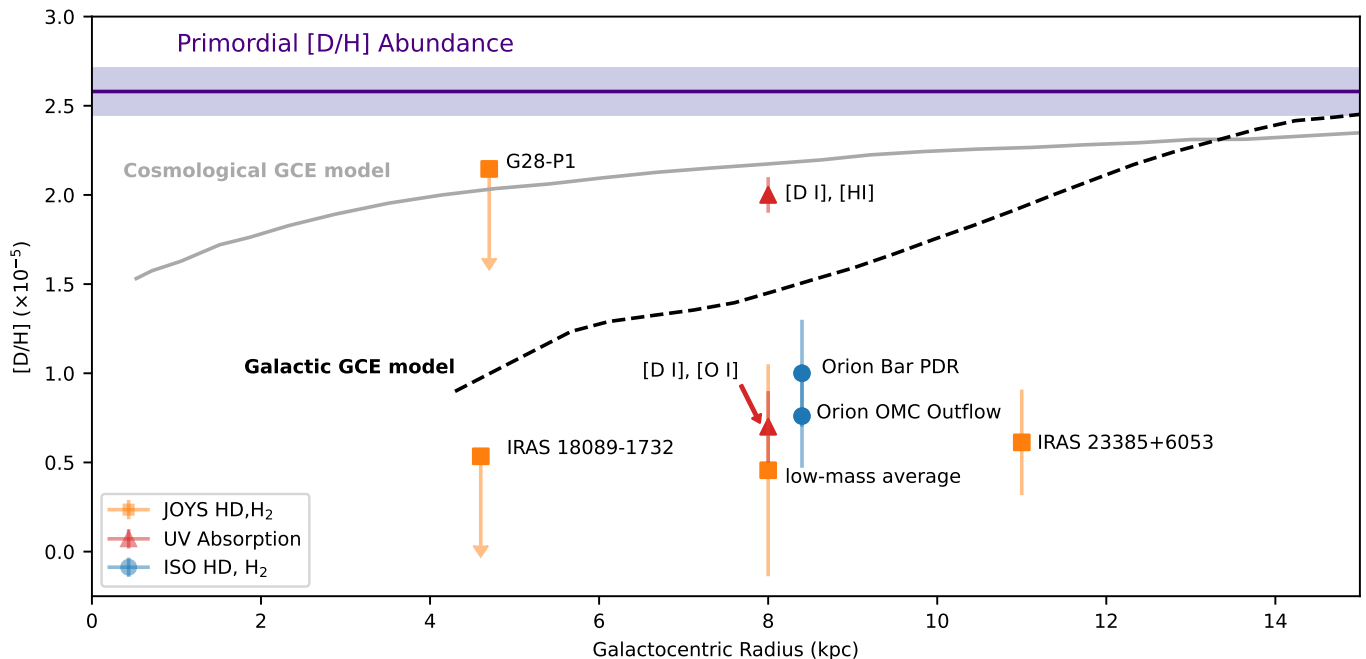


Fig. 7. $[D/H]$ as a function of Galactocentric radius based on our HD and H_2 rotational line measurements within JOYS (squares), other rotational line values from ISO (circles) (Wright et al. 1999; Bertoldi et al. 1999), and local Galactic disk values from UV absorption lines (triangles) (Prodanović et al. 2010; Hébrard 2010). Our measurements and those for the Orion OMC outflow include an upwards correction factor of 2.54 to $[D/H]$ for chemical conversion of HD to D. We also show Galactic chemical evolution models of our Galaxy from (black dashed line, reproduced from solid line in Fig. 5 of Romano et al. (2006)) and from a Milky Way type Galaxy in a cosmological zoom-in simulation from (grey line, reproduced from model 'm12i' in Fig. 5 of van de Voort et al. (2018)).

tions, and thus the atomic $[S\ I]$ and $[Fe\ I]$ lines are not tracing the solid reservoir into which deuterium is depleted.

An additional source of uncertainty in our $[D/H]$ measurements is the value of the chemical conversion and non-LTE correction factors derived by Bertoldi et al. (1999). While they show that the combination of these two correction factors is approximately constant across a range of shock conditions, more detailed modelling of individual spectra and shocks is warranted to see what fraction of our variations in $[D/H]$ can be attributed to differences in the excitation conditions and chemical conversion.

To make progress on measuring total $[D/H]$ with JWST, further work is needed on both the observations and modelling. On the observational front, deeper integrations would provide much better upper limits on the HD column density in quiescent regions of outflows where dust destruction is unlikely to occur. Observations of additional distant targets in the inner and outer Galaxy are needed, especially close to the Galactic center, if GCE models are to be constrained. In addition to protostellar outflows, rotational HD lines have also been detected in the IC 443C supernova remnant (Yuan et al. 2012). Observations of HD emission in supernova remnants may provide a useful probe of $[D/H]$ in higher velocity shock environments where grain destruction may be more complete. Observations with MIRI/MRS cover many rotational lines of H_2 and HD, but rovibrational transitions of both are found in the near-infrared accessible with NIRSpec. The additional rovibrational transitions would be useful for determining the shock conditions. Rovibrational transitions of HD have already been detected in PDRs (Peeters et al. 2024) with NIRSpec. Hints of Infrared emission bands from deuterated PAHs have been detected with JWST (Peeters et al. 2004, 2024), and their interpretation will be important for understanding their role as a reservoir for deuterium depletion.

In terms of modelling, it is particularly important to understand the shock conditions and degree of dust destruction. Shock models for H_2 (e.g. Kristensen et al. 2023) and forbidden atomic line emission (e.g. Hollenbach & McKee 1989) can be used to constrain the shock density, and velocity, and excitation conditions. (Caratti o Garatti et al. 2015, 2024). These are important inputs for determining the degree of non-LTE excitation and chemical conversion of HD that takes place in the shock positions.

6. Summary and Conclusions

Using JWST/MIRI observations from the JOYS program (PIDs: 1290, 1257) we have presented an analysis of rotational H_2 and HD lines in outflows from 5 high-mass and 5 low-mass protostars with the goal of constraining the $[D/H]$ abundance. Our results and conclusions can be summarized as follows:

- H_2 lines are detected towards all selected sources, but HD lines are only detected towards the brightest positions tracing the outflow shock knots in the low-mass sources, and in the one outer Galaxy ($R_{GC} = 11$ kpc) high-mass protostar IRAS 23385+6053. Notably, no HD emission is detected in the inner Galaxy high-mass protostars ($R_{GC} \sim 4$ kpc) where a higher degree of deuterium astration is expected.
- In resolved low-mass outflows, the morphology and flux of the HD emission is strongly correlated with high-excitation H_2 transitions, $[S\ I]$, and $[Fe\ I]$ line emission, showing a clear association with bright shock knots within the jet and bow-shocks.
- The column density or upper limits of H_2 and HD towards these sources has been obtained through an LTE rotation dia-

gram analysis. Additional corrections to the HD column density accounting for non-LTE behaviour and chemical conversion have been applied following Bertoldi et al. (1999). JWST/MIRI can now provide much more precise constraints on the H₂ and HD column density than previous facilities, thanks to the high sensitivity and large number of H₂ and HD lines in the mid-IR, which allow the excitation conditions to be more robustly constrained than previously possible.

- The H₂ rotation diagrams typically shows two components: a warm ($\sim 400\text{--}900\text{ K}$) and high column density ($\sim 10^{20} - 10^{22}\text{ cm}^{-2}$) component associated with the wide-angle outflows in the integrated line intensity maps, and a hot ($\sim 1000\text{--}2000\text{ K}$) and much lower column density component ($\sim 10^{17} - 10^{19}\text{ cm}^{-2}$) associated with bright knots and bow-shocks. In most cases the H₂ shows and ortho-to-para ratio of ~ 3 . For a handful of positions, an ortho-to-para ratio < 2.5 and evidence of enhanced excitation for the higher energy H₂ transitions is seen.
- The HD rotation diagrams are well-described by a single temperature component, and typically show column densities $\sim 10^5$ orders magnitude smaller than the warm H₂ component, and excitation temperatures intermediate between the warm and hot H₂ ($\sim 700 - 1000\text{ K}$.)
- Our derived [D/H] abundances show a factor of ~ 4 variation between low-mass protostar sources and between different positions within the same outflows. However, the gas compared between low-mass protostars and within a given outflow is expected to have experienced the same degree of astration. Furthermore, our abundances are a factor of $\sim 2\text{--}4$ below the predictions of GCE models. This suggests that we are not probing the total [D/H] in the observed protostars.
- The observed variations may be caused by the significant depletion of D into carbonaceous dust grains and varying degrees of grain destruction. The enhanced [D/H] and gas-phase abundance of Fe in the inner jet relative to the bow-shocks in HH 211 is consistent with this scenario.
- Most of our measurements of [D/H] or similar literature measurements using rotational lines suggest $[D/H] \lesssim 1.0 \times 10^{-5}$ over Galactocentric radii from 4.6 to 11 kpc, which is very difficult to reconcile with existing Galactic chemical evolution models while still satisfying other chemical abundance constraints. Depletion of D into dust and its release in shocks would be consistent with the variations in [D/H] between low-mass sources and the typically low values of [D/H] with respect to Galactic chemical evolution models. Further modeling of the effects of the grain destruction in the shocks are needed.

If the total [D/H] abundance can be accurately estimated, the detection of HD in IRAS 23385+6053 at a galactocentric distance of 11 kpc, and the upper limits in the inner Galaxy from IRAS 18089-1732 present an exciting opportunity. Additional observations of HD and H₂ in protostellar or supernova shocks when combined with models for the effects of depletion and chemical conversion could for the first time sample [D/H] across the Galactic disk, especially closer to the Galactic center and the outer Galaxy where little is known. This would provide powerful new constraints on models for the formation and chemical evolution of our Galaxy.

Acknowledgements. We are grateful to John H. Black for useful discussions on modelling of H₂ and HD emission, and to the anonymous referee for their comments on the paper. This work is based on observations made with the NASA/ESA/CSA James Webb Space Telescope. The data were obtained from the Mikulski Archive for Space Telescopes at the Space Telescope Science Institute, which is operated by the Association of Universities for Research in Astronomy, Inc., under NASA contract NAS 5-03127 for JWST. These observations are

associated with program 1290. Astrochemistry in Leiden is supported by funding from the European Research Council (ERC) under the European Union’s Horizon 2020 research and innovation programme (grant agreement No. 101019751 MOLDISK), by the Netherlands Research School for Astronomy (NOVA), and by grant TOP-1 614.001.751 from the Dutch Research Council (NWO). A.C.G. acknowledges support from PRIN-MUR 2022 20228JPA3A “The path to star and planet formation in the JWST era (PATH)” funded by NextGeneration EU and by INAF-GoG 2022 “NIR-dark Accretion Outbursts in Massive Young stellar objects (NAOMY)” and Large Grant INAF 2022 “YSOs Outflows, Disks and Accretion: towards a global framework for the evolution of planet forming systems (YODA)”. P.J.K. acknowledge support from the Science Foundation Ireland/Irish Research Council Pathway program under grant No. 21/PATH-S/9360

References

- Anderson, D. E., Bergin, E. A., Maret, S., & Wakelam, V. 2013, *ApJ*, 779, 141
- Awad, Z., Viti, S., Bayet, E., & Caselli, P. 2014, *MNRAS*, 443, 275
- Bergin, E. A., Cleeves, L. I., Crockett, N. R., Favre, C., & Neill, J. L. 2013, in *Astronomical Society of the Pacific Conference Series*, Vol. 476, *New Trends in Radio Astronomy in the ALMA Era: The 30th Anniversary of Nobeyama Radio Observatory*, ed. R. Kawabe, N. Kuno, & S. Yamamoto, 185
- Bertoldi, F., Timmermann, R., Rosenthal, D., Drapatz, S., & Wright, C. M. 1999, *A&A*, 346, 267
- Beuther, H., van Dishoeck, E. F., Tychoniec, L., et al. 2023, *A&A*, 673, A121
- Bushouse, H., Eisenhamer, J., Dencheva, N., et al. 2024, *JWST Calibration Pipeline*
- Caratti o Garatti, A., Ray, T. P., Kavanagh, P. J., et al. 2024, *A&A*, 691, A134
- Caratti o Garatti, A., Stecklum, B., Linz, H., Garcia Lopez, R., & Sanna, A. 2015, *A&A*, 573, A82
- Ceccarelli, C., Caselli, P., Bockelée-Morvan, D., et al. 2014, in *Protostars and Planets VI*, ed. H. Beuther, R. S. Klessen, C. P. Dullemond, & T. Henning, 859–882
- Chiappini, C., Matteucci, F., & Romano, D. 2001, *ApJ*, 554, 1044
- Chiappini, C., Renda, A., & Matteucci, F. 2002, *A&A*, 395, 789
- Christiaens, V., Gonzalez, C., Farkas, R., et al. 2023, *The Journal of Open Source Software*, 8, 4774
- Cooke, R. J., Pettini, M., Jorgenson, R. A., Murphy, M. T., & Steidel, C. C. 2014, *ApJ*, 781, 31
- Cybart, R. H., Fields, B. D., Olive, K. A., & Yeh, T.-H. 2016, *Reviews of Modern Physics*, 88, 015004
- Draine, B. T. 2006, in *Astronomical Society of the Pacific Conference Series*, Vol. 348, *Astrophysics in the Far Ultraviolet: Five Years of Discovery with FUSE*, ed. G. Sonneborn, H. W. Moos, & B. G. Andersson, 58
- Epstein, R. I., Lattimer, J. M., & Schramm, D. N. 1976, *Nature*, 263, 198
- Friedman, S. D., Chayer, P., Jenkins, E. B., et al. 2023, *ApJ*, 946, 34
- Giannini, T., Antonucci, S., Nisini, B., Bacciotti, F., & Podio, L. 2015, *ApJ*, 814, 52
- Giannini, T., Calzoletti, L., Nisini, B., et al. 2008, *A&A*, 481, 123
- Giannini, T., Nisini, B., Neufeld, D., et al. 2011, in *IAU Symposium*, Vol. 280, *The Molecular Universe*, ed. J. Cernicharo & R. Bachiller, 329
- Gieser, C., Beuther, H., van Dishoeck, E. F., et al. 2023, *A&A*, 679, A108
- Greenfield, P. & Miller, T. 2016, *Astronomy and Computing*, 16, 41
- Hébrard, G. 2010, in *Light Elements in the Universe*, ed. C. Charbonnel, M. Tosi, F. Primas, & C. Chiappini, Vol. 268, 59–64
- Hébrard, G. & Moos, H. W. 2003, *ApJ*, 599, 297
- Hollenbach, D. & McKee, C. F. 1989, *ApJ*, 342, 306
- Hoopes, C. G., Sembach, K. R., Hébrard, G., Moos, H. W., & Knauth, D. C. 2003, *ApJ*, 586, 1094
- Jenkins, E. B. 2009, *ApJ*, 700, 1299
- Jura, M. 1982, in *NASA Conference Publication*, Vol. 2238, *NASA Conference Publication*, ed. Y. Kondo, 54–60
- Kama, M., Shorttle, O., Jermyn, A. S., et al. 2019, *ApJ*, 885, 114
- Kristensen, L. E., Godard, B., Guillard, P., Gusdorf, A., & Pineau des Forêts, G. 2023, *A&A*, 675, A86
- Le Gouellec, V. J. M., Lew, B. W. P., Greene, T. P., et al. 2024, *arXiv e-prints*, submitted to *ApJ*, arXiv:2410.11095
- Linsky, J. L., Draine, B. T., Moos, H. W., et al. 2006, *ApJ*, 647, 1106
- Lubowich, D. A., Pasachoff, J. M., Balonek, T. J., et al. 2000, *Nature*, 405, 1025
- Mangum, J. G. & Shirley, Y. L. 2015, *PASP*, 127, 266
- McClure, M. K., Bergin, E. A., Cleeves, L. I., et al. 2016, *ApJ*, 831, 167
- Narang, M., Manoj, P., Tyagi, H., et al. 2024, *ApJ*, 962, L16
- Neufeld, D. A., Green, J. D., Hollenbach, D. J., et al. 2006a, *ApJ*, 647, L33
- Neufeld, D. A., Melnick, G. J., & Harwit, M. 1998, *ApJ*, 506, L75
- Neufeld, D. A., Melnick, G. J., Sonnentrucker, P., et al. 2006b, *ApJ*, 649, 816
- Nisini, B., Bacciotti, F., Giannini, T., et al. 2005, *A&A*, 441, 159
- Peeters, E., Allamandola, L. J., Bauschlicher, C. W., J., et al. 2004, *ApJ*, 604, 252

- Peeters, E., Habart, E., Berné, O., et al. 2024, A&A, 685, A74
- Penzias, A. A. 1979, ApJ, 228, 430
- Penzias, A. A., Wannier, P. G., Wilson, R. H., & Linke, R. A. 1977, ApJ, 211, 108
- Podio, L., Bacciotti, F., Nisini, B., et al. 2006, A&A, 456, 189
- Polehampton, E. T., Baluteau, J. P., Ceccarelli, C., Swinyard, B. M., & Caux, E. 2002, A&A, 388, L44
- Pontoppidan, K. M., Evans, N., Bergner, J., & Yang, Y.-L. 2024, Research Notes of the American Astronomical Society, 8, 68
- Prantzos, N. 1996, A&A, 310, 106
- Prodanović, T., Steigman, G., & Fields, B. D. 2010, MNRAS, 406, 1108
- Romano, D., Tosi, M., Chiappini, C., & Matteucci, F. 2006, MNRAS, 369, 295
- Romano, D., Tosi, M., Matteucci, F., & Chiappini, C. 2003, MNRAS, 346, 295
- Sarkar, S. 1996, Reports on Progress in Physics, 59, 1493
- Tielens, A. G. G. M. 1983, A&A, 119, 177
- Tielens, A. G. G. M. 2008, ARA&A, 46, 289
- Tielens, A. G. G. M. 2013, Reviews of Modern Physics, 85, 1021
- Tosi, M. 2010, in Light Elements in the Universe, ed. C. Charbonnel, M. Tosi, F. Primas, & C. Chiappini, Vol. 268, 153–161
- Tsujimoto, T. 2011, MNRAS, 410, 2540
- Tsujimoto, T., Bland-Hawthorn, J., & Freeman, K. C. 2010, PASJ, 62, 447
- van de Voort, F., Quataert, E., Faucher-Giguère, C.-A., et al. 2018, MNRAS, 477, 80
- van Dishoeck, E. F. 2004, ARA&A, 42, 119
- van Dishoeck, E. F., Wright, C. M., Cernicharo, J., et al. 1998, ApJ, 502, L173
- Wooten, A. 1987, in Astrochemistry, ed. M. S. Vardya & S. P. Tarafdar, Vol. 120, 311–319
- Wright, C. M., van Dishoeck, E. F., Cox, P., Sidher, S. D., & Kessler, M. F. 1999, ApJ, 515, L29
- Yuan, Y. & Neufeld, D. A. 2011, ApJ, 726, 76
- Yuan, Y., Neufeld, D. A., Sonnentrucker, P., Melnick, G. J., & Watson, D. M. 2012, ApJ, 753, 126

Appendix A: Analyzed Spectral Lines

We report the H₂, HD, and forbidden atomic lines analyzed in this work in Table A.1.

Table A.1. Analyzed H₂, HD, and forbidden atomic lines.

Species	Transition	λ (μm)	E_{up} (K)	A_{ul} (s^{-1})
HD	(0,0) R(9)	12.4805	6656.3	4.97×10^{-5}
HD	(0,0) R(8)	13.5961	5503.5	3.87×10^{-5}
HD	(0,0) R(7)	15.2510	4445.2	2.88×10^{-5}
HD	(0,0) R(6)	16.8938	3487.4	2.03×10^{-5}
HD	(0,0) R(5)	19.4310	2635.8	1.33×10^{-5}
HD	(0,0) R(4)	23.0338	1895.3	7.91×10^{-6}
H ₂	(0,0) S(8)	5.0531	8677.1	3.23×10^{-7}
H ₂	(0,0) S(7)	5.5111	7196.7	2.00×10^{-7}
H ₂	(0,0) S(6)	6.1086	5829.8	1.14×10^{-7}
H ₂	(0,0) S(5)	6.9095	4586.1	5.88×10^{-8}
H ₂	(0,0) S(4)	8.0250	3474.5	2.64×10^{-8}
H ₂	(0,0) S(3)	9.6649	2503.7	9.83×10^{-9}
H ₂	(0,0) S(2)	12.2786	1681.6	2.75×10^{-9}
H ₂	(0,0) S(1)	17.0348	1015.1	4.76×10^{-10}
[S I]	³ P ₁ - ³ P ₂	25.2490	569.83	8.27×10^{-9}
[Fe I]	a ⁵ D ₃ -a ⁵ D ₄	24.0423	598.43	2.51×10^{-3}
[Fe II]	a ⁴ F _{7/2} -a ⁴ F _{9/2}	17.9359	3496.42	5.86×10^{-3}

Appendix B: Aperture Locations

We describe the position of the apertures used for spectral extraction towards each source in Table B.1.

Table B.1. Position of our extracted aperture centers in each source. Each aperture is 1'' in radius.

Source	Aperture	RA (J200)	Dec (J2000)
G28-IRS2	1	18:42:51.89	-3:59:53.0
G28-P1-A	1	18:42:50.72	-4:03:16.9
G31-A	1	18:47:34.31	-1:12:45.0
IRAS 18089-1732	1	18:11:51.47	-17:31:24.8
IRAS 23385+6053	1	23:40:54.80	+61:10:28.5
BHR71-IRS1	1	12:01:36.40	-65:08:51.5
BHR71-IRS1	2	12:01:36.48	-65:08:53.5
BHR71-IRS1	3	12:01:36.36	-65:08:55.5
BHR71-IRS1	4	12:01:36.43	-65:08:57.6
HH 211	1	3:43:57.34	32:00:46.9
HH 211	2	3:43:57.52	32:00:45.6
HH 211	3	3:43:57.76	32:00:44.3
HH 211	4	3:43:58.26	32:00:41.6
HH 211	5	3:43:58.59	32:00:41.5
HH 211	6	3:43:58.90	32:00:35.6
HH 211	7	3:43:59.39	32:00:35.1
HH 211	8	3:43:59.64	32:00:34.1
HH 211	9	3:43:59.88	32:00:34.4
IRAS 4B	1	3:29:12.05	31:13:02.1
IRAS 4B	2	3:29:12.09	31:13:00.7
L1448-mm	1	3:25:38.82	30:44:07.5
L1448-mm	2	3:25:38.74	30:44:09.3
L1448-mm	3	3:25:38.67	30:44:11.2
L1448-mm	4	3:25:38.57	30:44:09.3
Ser-emb 8 (N)	1	18:29:49.34	1:16:52.0
Ser-emb 8 (N)	2	18:29:49.19	1:16:53.1

Appendix C: Integrated Line Intensity Maps

We show below the integrated line intensity maps for all sources in Table 1 except IRAS 23385+6053 and HH211, which are shown in Sect. 3.1.

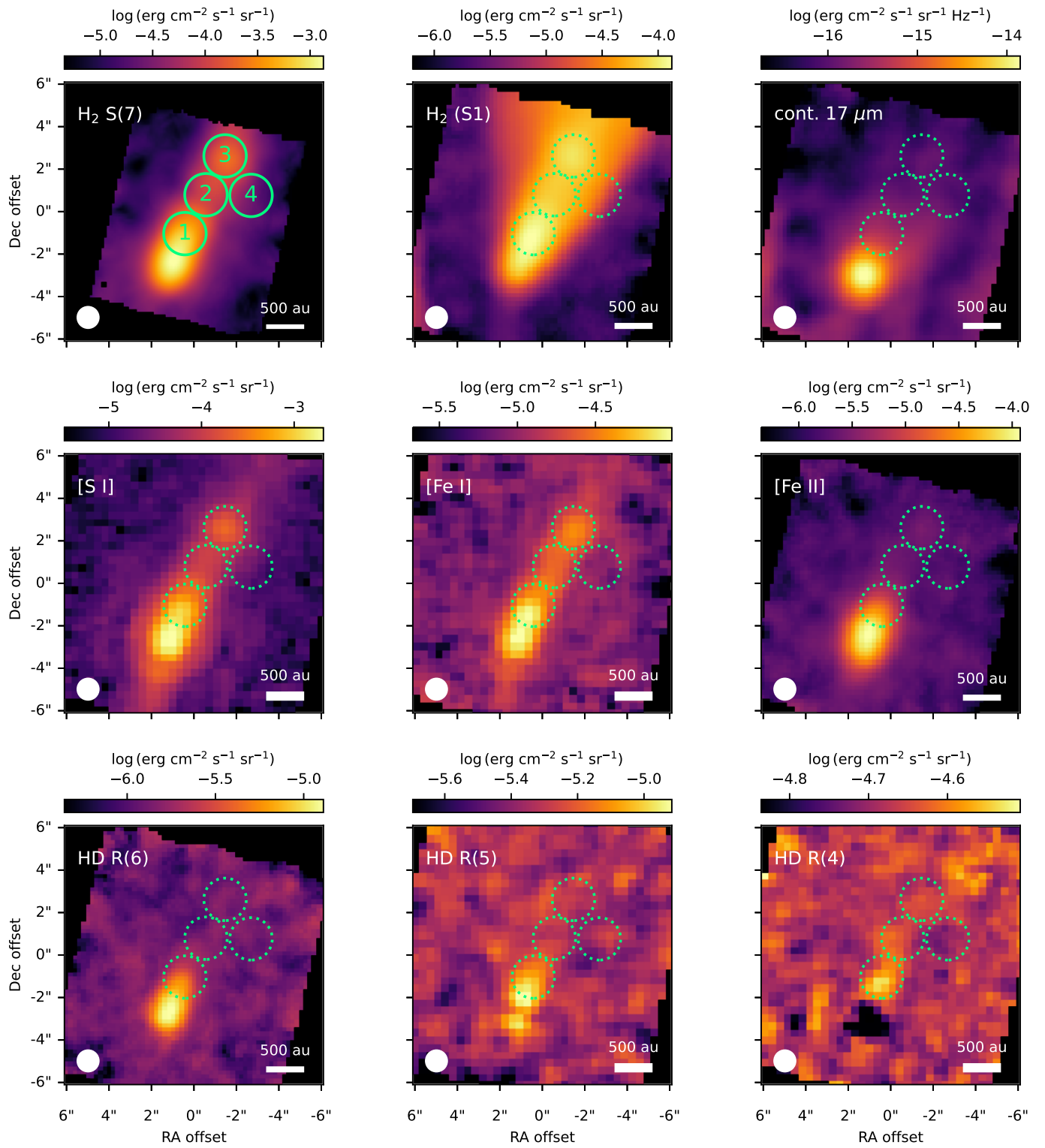


Fig. C.1. Same as Fig. 1, but for L1448-mm.

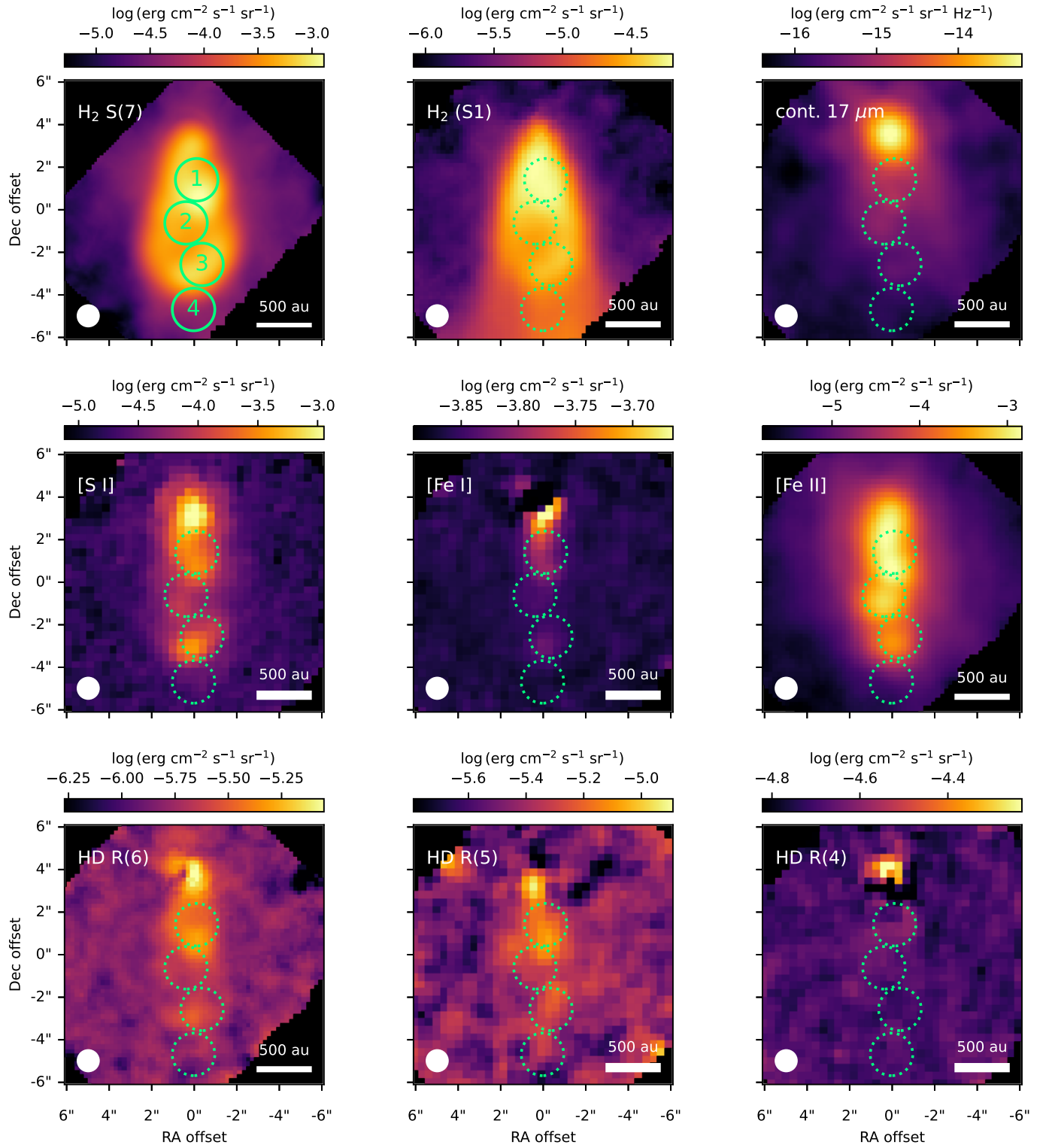


Fig. C.2. Same as Fig. 1, but for BHR71-IRS1.

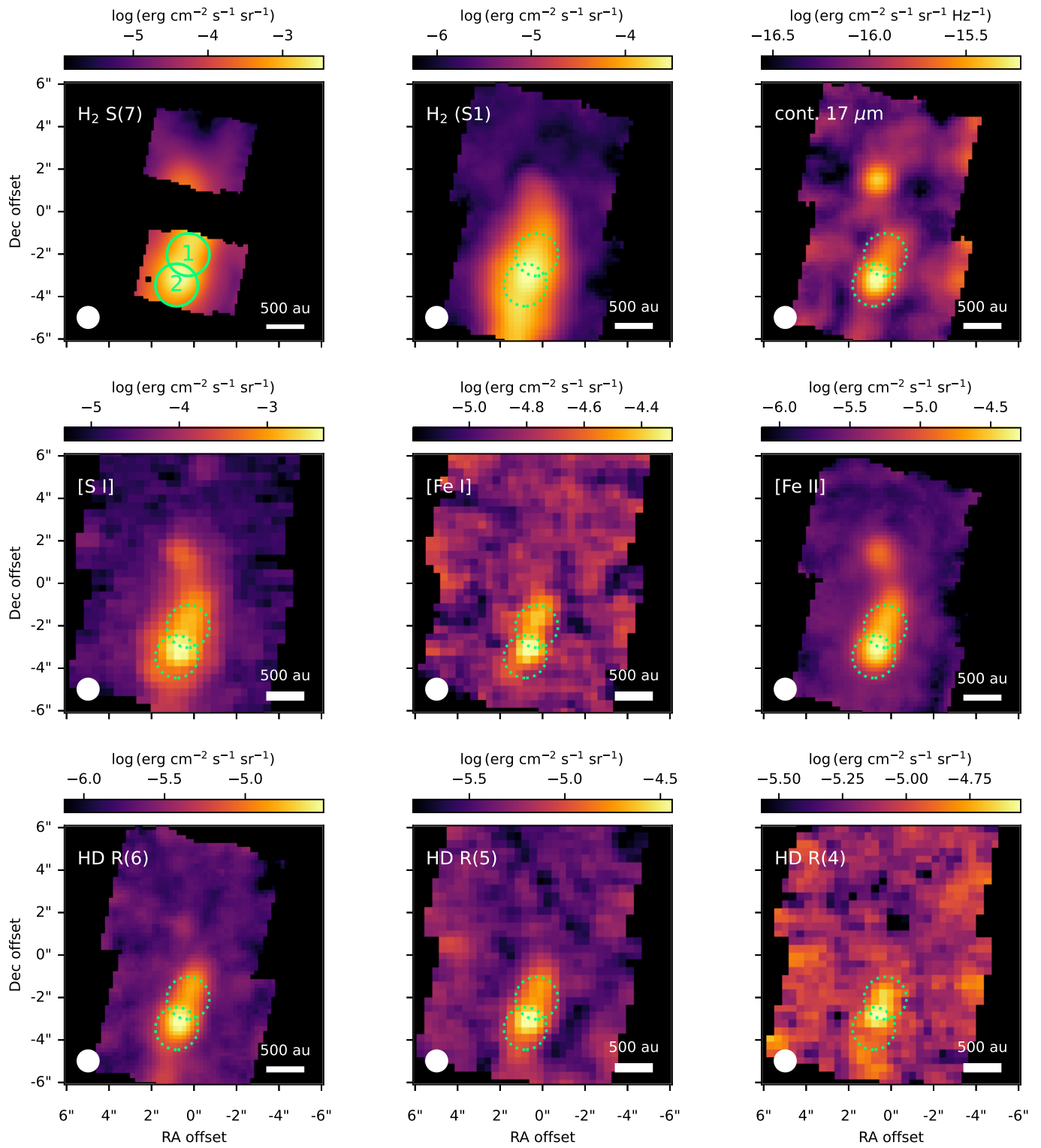


Fig. C.3. Same as Fig. 1, but for IRAS4B.

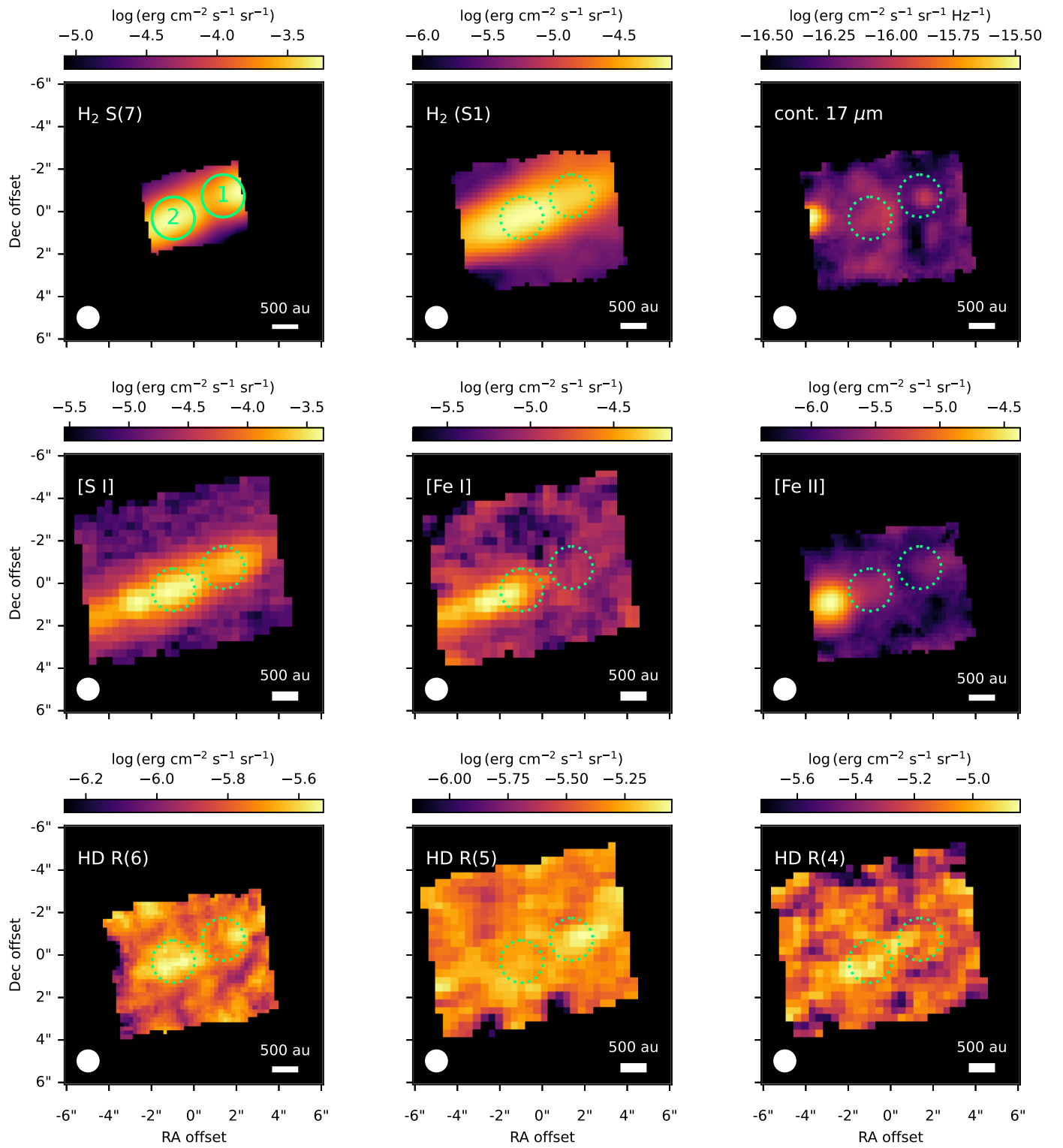


Fig. C.4. Same as Fig. 1, but for Ser-emb8N.

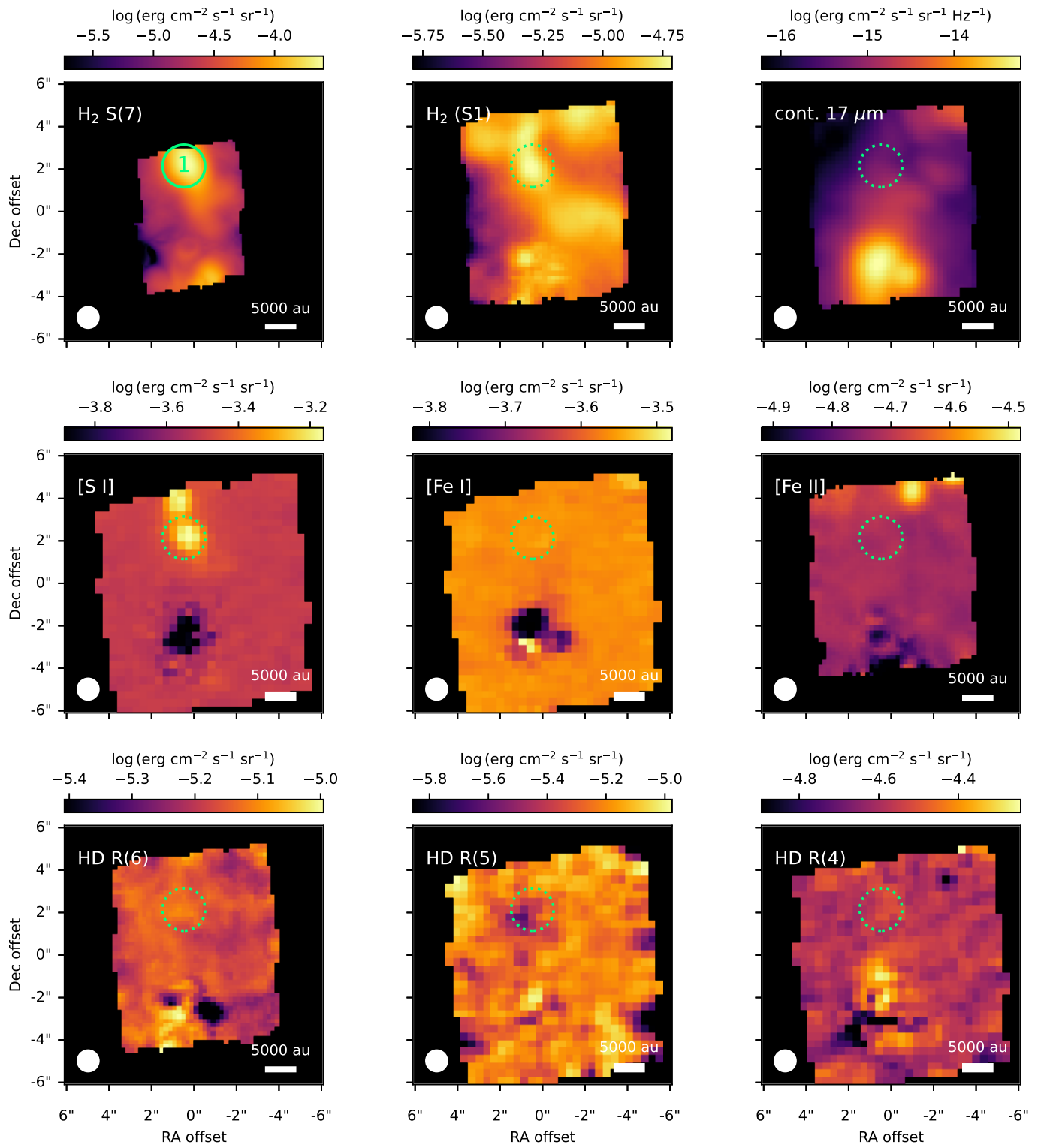


Fig. C.5. Same as Fig. 1, but for IRAS 18089-1732.

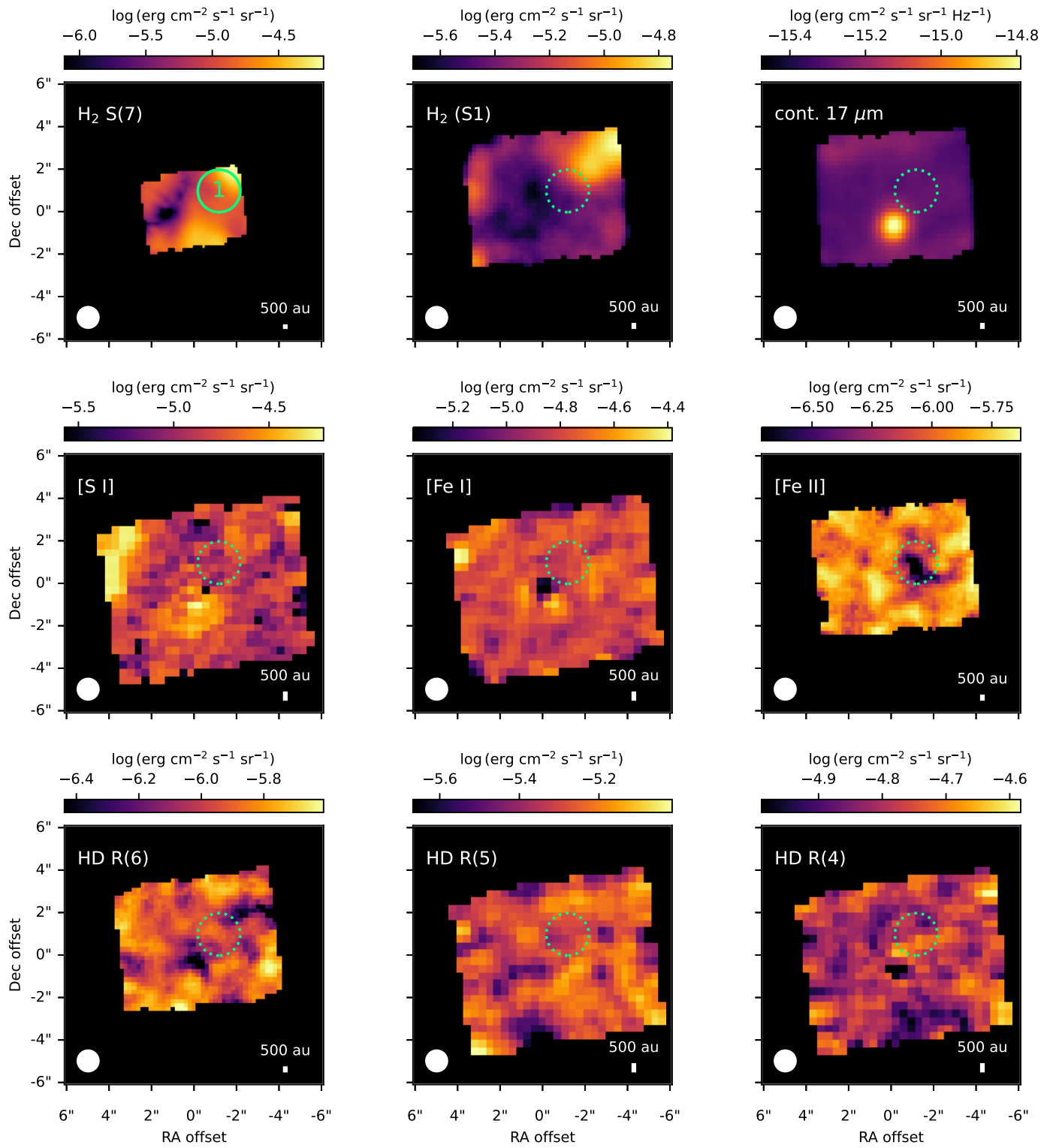


Fig. C.6. Same as Fig. 1, but for G28-IRS2.

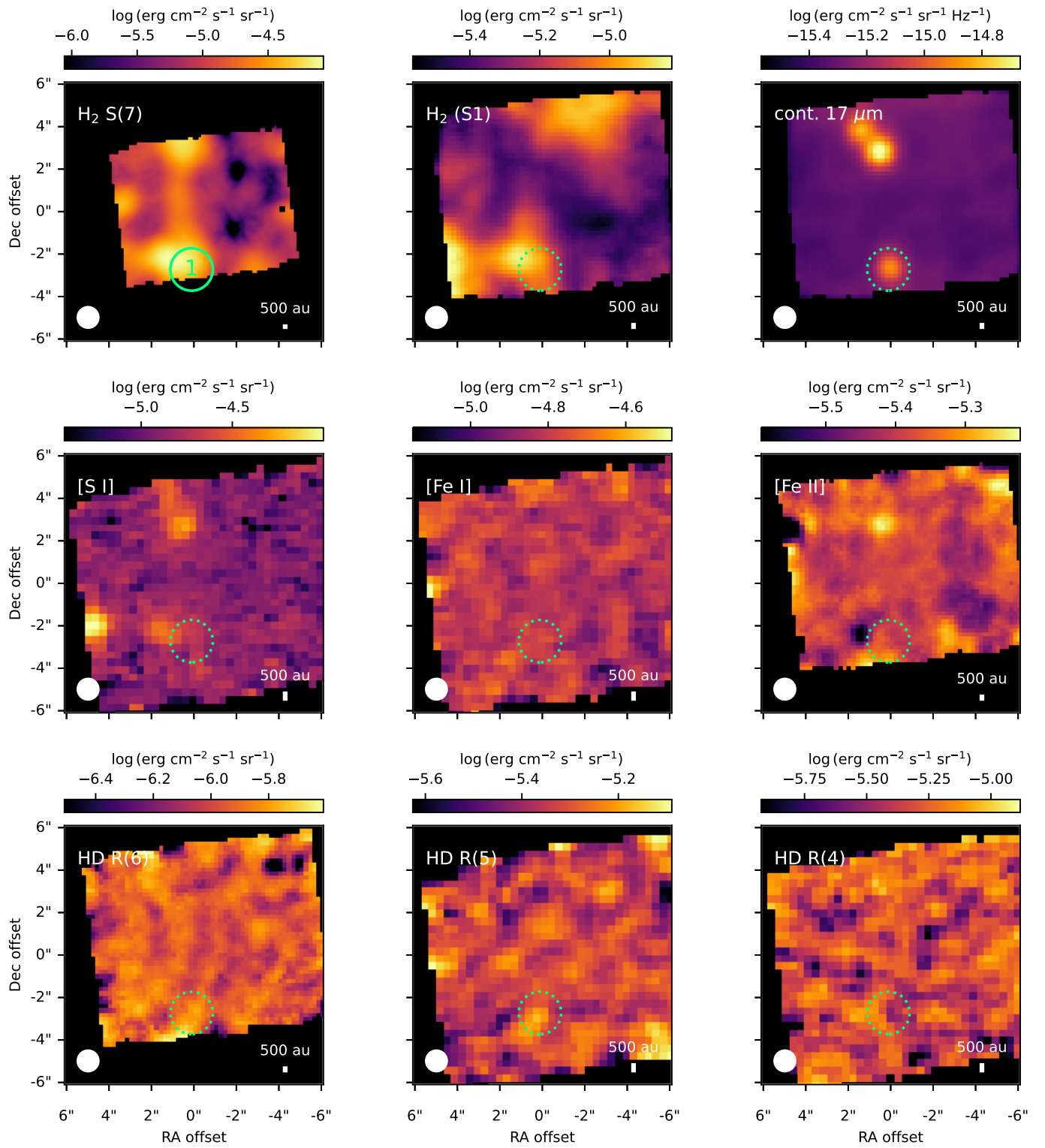


Fig. C.7. Same as Fig. 1, but for G28-P1.

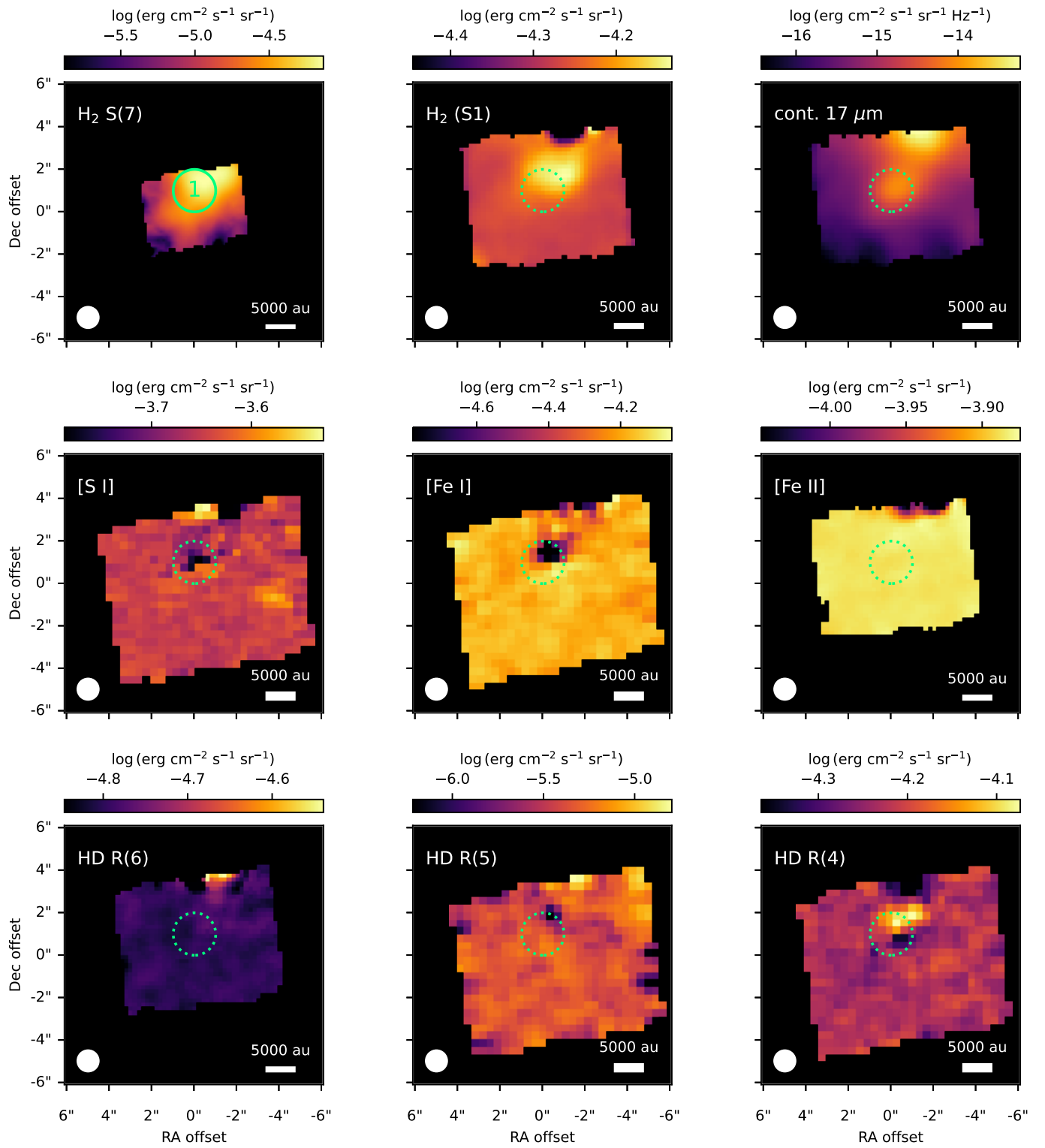


Fig. C.8. Same as Fig. 1, but for G31.

Appendix D: Example H₂ and HD line detections

In Figure D.1, we show additional examples of detected H₂, HD, and selected atomic lines.

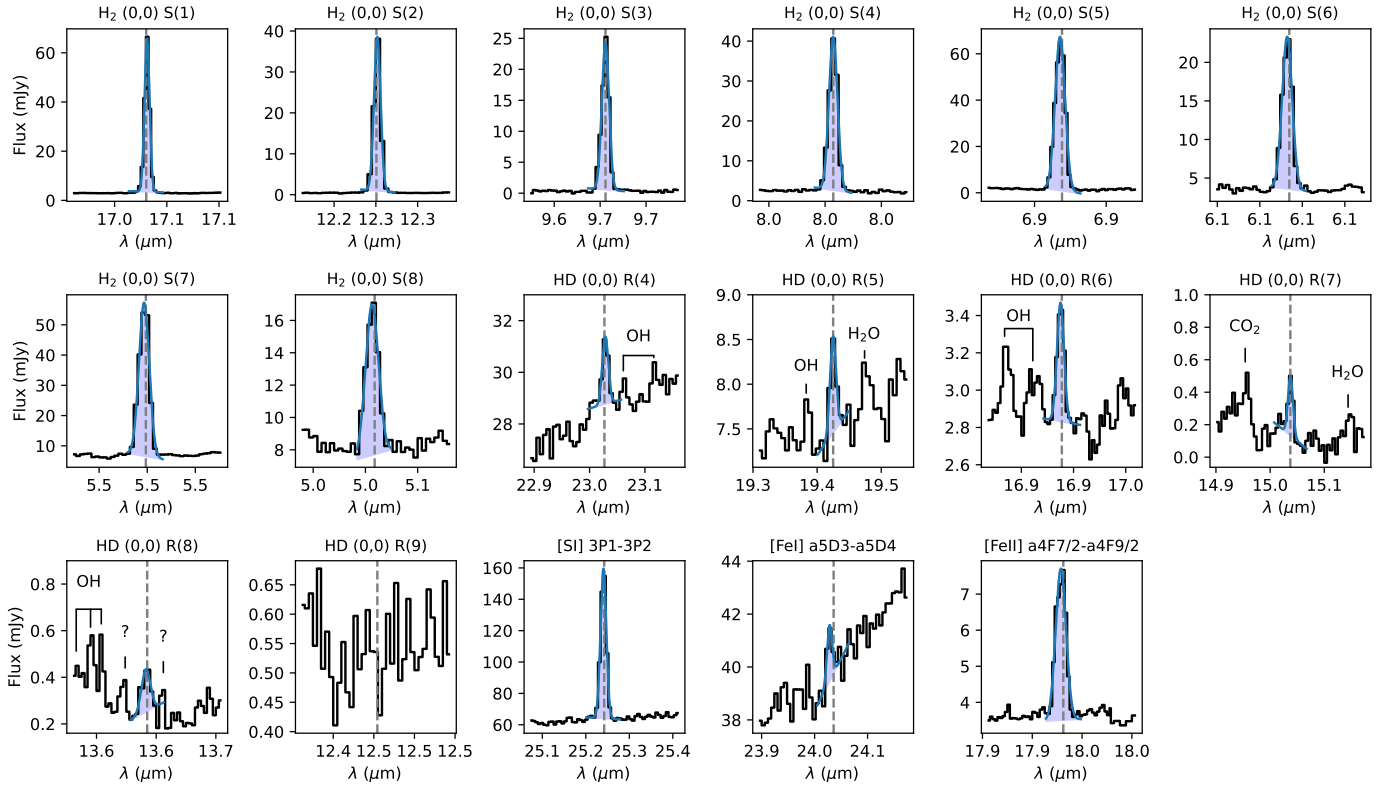


Fig. D.1. Same as Fig. 3, but for IRAS 23385+6053 aperture 1.

Appendix E: Line Fluxes

In Tables E.1 to E.3 we provide the H₂, HD, and atomic line fluxes or upper limits for every aperture in Table B.1.

Table E.1. H₂ Line fluxes and upper limits, units of 10⁻¹⁵ erg cm⁻² s⁻¹. No extinction correction is applied.

Source	Ap.	H ₂ S(1)	H ₂ S(2)	H ₂ S(3)	H ₂ S(4)	H ₂ S(5)	H ₂ S(6)	H ₂ S(7)	H ₂ S(8)
G28-IRS2	1	0.96 ± 0.02	0.36 ± 0.01	0.19 ± 0.03	0.57 ± 0.01	0.53 ± 0.04	< 0.09	1.70 ± 0.10	0.28 ± 0.03
G28-P1-A	1	1.04 ± 0.03	0.65 ± 0.02	0.28 ± 0.02	1.38 ± 0.04	1.93 ± 0.04	0.48 ± 0.03	2.91 ± 0.06	0.68 ± 0.03
G31-A	1	1.66 ± 0.05	1.64 ± 0.02	0.09 ± 0.02	2.47 ± 0.06	2.38 ± 0.08	0.52 ± 0.02	3.40 ± 0.07	0.63 ± 0.04
IRAS 18089-1732	1	1.52 ± 0.05	1.58 ± 0.02	0.18 ± 0.01	5.38 ± 0.07	7.93 ± 0.04	1.96 ± 0.02	10.72 ± 0.05	2.11 ± 0.03
IRAS 23385+6053	1	3.92 ± 0.07	3.68 ± 0.12	2.99 ± 0.21	6.79 ± 0.39	14.45 ± 1.02	4.71 ± 0.42	13.45 ± 1.31	3.40 ± 0.51
BHR71-IRS1	1	3.95 ± 0.02	5.51 ± 0.12	10.50 ± 0.06	23.49 ± 0.27	55.30 ± 0.57	17.15 ± 0.16	57.26 ± 0.93	13.94 ± 0.27
BHR71-IRS1	2	2.47 ± 0.03	3.78 ± 0.11	12.97 ± 0.10	14.02 ± 0.17	40.16 ± 0.53	12.96 ± 0.13	42.25 ± 0.33	11.77 ± 0.15
BHR71-IRS1	3	2.12 ± 0.02	3.13 ± 0.06	15.86 ± 0.25	12.69 ± 0.34	39.33 ± 1.02	13.41 ± 0.32	42.37 ± 1.32	14.53 ± 0.32
BHR71-IRS1	4	1.08 ± 0.01	1.11 ± 0.02	4.02 ± 0.05	2.22 ± 0.04	5.64 ± 0.11	1.61 ± 0.08	5.31 ± 0.12	1.47 ± 0.06
HH 211	1	6.62 ± 0.18	7.57 ± 0.29	26.67 ± 0.33	17.26 ± 0.16	41.01 ± 0.89	9.85 ± 0.14	21.27 ± 0.19	4.47 ± 0.08
HH 211	2	6.89 ± 0.15	6.44 ± 0.04	21.32 ± 0.38	10.29 ± 0.10	21.97 ± 0.69	4.98 ± 0.07	9.24 ± 0.08	1.98 ± 0.11
HH 211	3	7.54 ± 0.16	6.98 ± 0.02	25.00 ± 0.36	12.59 ± 0.13	27.77 ± 0.58	6.25 ± 0.14	11.83 ± 0.12	2.27 ± 0.08
HH 211	4	2.71 ± 0.08	2.95 ± 0.04	8.69 ± 0.13	3.96 ± 0.07	8.29 ± 0.11	1.84 ± 0.05	4.00 ± 0.07	1.01 ± 0.06
HH 211	5	1.83 ± 0.04	3.46 ± 0.06	7.27 ± 0.07	5.22 ± 0.05	8.76 ± 0.13	2.35 ± 0.05	4.74 ± 0.10	1.22 ± 0.07
HH 211	6	1.72 ± 0.08	2.15 ± 0.03	5.88 ± 0.06	2.61 ± 0.06	5.08 ± 0.17	1.29 ± 0.04	2.75 ± 0.12	0.50 ± 0.09
HH 211	7	13.69 ± 0.46	45.55 ± 0.32	63.86 ± 1.79	67.14 ± 0.70	120.38 ± 1.20	46.32 ± 1.06	98.16 ± 0.92	30.25 ± 0.72
HH 211	8	6.44 ± 0.19	12.25 ± 0.13	38.03 ± 0.87	28.68 ± 0.40	77.85 ± 1.32	24.82 ± 0.57	65.23 ± 0.59	20.78 ± 0.67
HH 211	9	4.72 ± 0.14	12.19 ± 0.22	27.32 ± 0.52	26.92 ± 0.27	66.47 ± 1.59	28.50 ± 0.37	66.35 ± 0.50	26.72 ± 1.22
IRAS 4B	1	11.36 ± 0.42	18.70 ± 0.22	16.27 ± 0.09	52.84 ± 0.75	91.97 ± 1.56	36.45 ± 0.69	103.99 ± 0.63	33.24 ± 0.68
IRAS 4B	2	14.88 ± 0.49	24.38 ± 0.23	22.95 ± 0.13	62.85 ± 0.81	99.36 ± 1.01	45.21 ± 0.67	113.75 ± 1.15	34.98 ± 0.64
L1448-mm	1	7.26 ± 0.09	6.93 ± 0.04	25.01 ± 0.17	20.36 ± 0.13	47.42 ± 0.57	11.82 ± 0.07	35.52 ± 0.39	7.42 ± 0.12
L1448-mm	2	4.78 ± 0.03	4.43 ± 0.05	15.53 ± 0.11	8.45 ± 0.12	17.10 ± 0.31	3.54 ± 0.05	7.55 ± 0.11	1.39 ± 0.07
L1448-mm	3	5.35 ± 0.04	5.63 ± 0.06	19.72 ± 0.16	10.15 ± 0.12	21.47 ± 0.28	4.54 ± 0.05	9.98 ± 0.13	2.04 ± 0.12
L1448-mm	4	1.77 ± 0.03	1.70 ± 0.01	5.11 ± 0.05	2.68 ± 0.06	4.53 ± 0.07	0.84 ± 0.04	1.93 ± 0.10	0.40 ± 0.03
Ser-emb 8 (N)	1	2.96 ± 0.02	6.71 ± 0.05	6.29 ± 0.06	17.19 ± 0.20	28.85 ± 0.54	10.27 ± 0.23	22.88 ± 0.19	6.43 ± 0.10
Ser-emb 8 (N)	2	4.45 ± 0.02	9.13 ± 0.05	10.07 ± 0.11	21.46 ± 0.20	42.65 ± 0.36	11.80 ± 0.09	28.69 ± 0.30	7.16 ± 0.23

Table E.2. HD Line fluxes and upper limits, units of 10^{-15} erg cm $^{-2}$ s $^{-1}$. No extinction correction is applied.

Source	Aperture	HD R(4)	HD R(5)	HD R(6)	HD R(7)	HD R(8)	HD R(9)
G28-IRS2	1	< 0.12	< 0.04	< 0.02	< 0.02	< 0.02	< 0.02
G28-P1-A	1	< 0.09	< 0.03	< 0.02	< 0.03	< 0.03	< 0.02
G31-A	1	< 0.92	< 0.15	< 0.03	< 0.25	< 0.04	< 0.03
IRAS 18089-1732	1	< 0.16	< 0.07	< 0.02	< 0.10	< 0.05	< 0.03
IRAS 23385+6053	1	0.20 ± 0.03	0.10 ± 0.02	0.06 ± 0.00	0.03 ± 0.00	0.03 ± 0.01	< 0.01
BHR71-IRS1	1	0.29 ± 0.09	0.21 ± 0.05	0.18 ± 0.01	0.07 ± 0.00	0.05 ± 0.01	0.05 ± 0.01
BHR71-IRS1	2	0.16 ± 0.03	0.10 ± 0.02	0.09 ± 0.01	0.06 ± 0.01	0.03 ± 0.00	0.03 ± 0.01
BHR71-IRS1	3	< 0.10	0.08 ± 0.02	0.08 ± 0.01	0.05 ± 0.00	0.03 ± 0.00	0.07 ± 0.02
BHR71-IRS1	4	< 0.07	< 0.05	< 0.02	< 0.03	< 0.02	< 0.02
HH 211	1	0.22 ± 0.03	0.13 ± 0.03	0.08 ± 0.01	0.06 ± 0.01	< 0.03	< 0.02
HH 211	2	0.18 ± 0.05	0.09 ± 0.02	0.03 ± 0.01	< 0.03	< 0.03	< 0.02
HH 211	3	0.22 ± 0.04	0.10 ± 0.01	0.05 ± 0.01	0.01 ± 0.01	< 0.03	< 0.03
HH 211	4	< 0.11	< 0.05	< 0.02	< 0.03	< 0.03	< 0.02
HH 211	5	< 0.13	< 0.08	< 0.02	< 0.02	< 0.02	< 0.02
HH 211	6	< 0.12	< 0.08	< 0.03	< 0.05	< 0.04	< 0.03
HH 211	7	0.93 ± 0.10	0.61 ± 0.08	0.37 ± 0.04	0.21 ± 0.02	0.13 ± 0.01	0.10 ± 0.02
HH 211	8	0.32 ± 0.04	0.29 ± 0.07	0.20 ± 0.02	0.13 ± 0.01	0.09 ± 0.01	0.09 ± 0.01
HH 211	9	0.19 ± 0.11	0.85 ± 0.69	0.25 ± 0.05	0.20 ± 0.02	0.12 ± 0.01	0.09 ± 0.02
IRAS 4B	1	0.83 ± 0.29	0.60 ± 0.20	0.74 ± 0.10	0.26 ± 0.02	0.29 ± 0.05	0.19 ± 0.02
IRAS 4B	2	0.89 ± 0.39	0.66 ± 0.25	0.97 ± 0.16	0.39 ± 0.03	0.34 ± 0.08	0.25 ± 0.03
L1448-mm	1	0.39 ± 0.02	0.22 ± 0.04	0.15 ± 0.01	0.10 ± 0.00	0.03 ± 0.01	0.03 ± 0.01
L1448-mm	2	0.12 ± 0.02	0.05 ± 0.02	0.02 ± 0.00	< 0.02	< 0.01	< 0.01
L1448-mm	3	0.13 ± 0.02	0.04 ± 0.02	0.02 ± 0.01	< 0.02	< 0.01	< 0.01
L1448-mm	4	< 0.09	< 0.04	< 0.02	< 0.02	< 0.01	< 0.01
Ser-emb 8 (N)	1	0.20 ± 0.07	0.15 ± 0.04	0.09 ± 0.01	< 0.03	< 0.02	< 0.02
Ser-emb 8 (N)	2	0.33 ± 0.05	0.14 ± 0.02	0.12 ± 0.01	0.04 ± 0.01	0.02 ± 0.01	0.03 ± 0.01

Table E.3. Atomic Line fluxes and upper limits, units of 10^{-15} erg cm $^{-2}$ s $^{-1}$. No extinction correction is applied.

Source	Aperture	[SI] 3P1-3P2	[FeI] a5D3-a5D4	[FeII] a4F7/2-a4F9/2
G28-IRS2	1	0.35 ± 0.08	< 0.16	< 0.02
G28-P1-A	1	0.65 ± 0.08	< 0.13	< 0.02
G31-A	1	< 3.16	< 1.32	< 0.04
IRAS 18089-1732	1	14.29 ± 0.52	< 0.29	< 0.03
IRAS 23385+6053	1	7.47 ± 0.13	0.13 ± 0.05	0.51 ± 0.06
BHR71-IRS1	1	19.43 ± 0.34	1.69 ± 0.14	81.71 ± 3.30
BHR71-IRS1	2	6.59 ± 0.09	0.68 ± 0.06	55.90 ± 1.22
BHR71-IRS1	3	11.82 ± 0.28	0.56 ± 0.04	12.89 ± 0.13
BHR71-IRS1	4	1.34 ± 0.05	< 0.12	0.91 ± 0.00
HH 211	1	13.38 ± 0.75	2.31 ± 0.15	0.12 ± 0.01
HH 211	2	4.47 ± 0.24	0.64 ± 0.07	0.03 ± 0.01
HH 211	3	7.78 ± 0.44	1.55 ± 0.06	0.08 ± 0.01
HH 211	4	0.66 ± 0.07	< 0.17	< 0.03
HH 211	5	< 0.16	< 0.17	< 0.02
HH 211	6	< 0.23	< 0.22	< 0.03
HH 211	7	23.76 ± 1.13	0.28 ± 0.06	7.29 ± 0.04
HH 211	8	15.72 ± 0.61	< 0.25	1.47 ± 0.02
HH 211	9	20.61 ± 0.81	< 0.26	2.66 ± 0.06
IRAS 4B	1	100.04 ± 3.48	1.33 ± 0.10	1.38 ± 0.05
IRAS 4B	2	142.39 ± 10.32	1.31 ± 0.13	1.46 ± 0.06
L1448-mm	1	41.88 ± 1.58	3.15 ± 0.18	1.30 ± 0.03
L1448-mm	2	8.16 ± 0.36	1.24 ± 0.07	0.07 ± 0.00
L1448-mm	3	9.81 ± 0.59	1.42 ± 0.07	0.07 ± 0.01
L1448-mm	4	1.51 ± 0.09	0.18 ± 0.04	< 0.03
Ser-emb 8 (N)	1	11.21 ± 0.44	0.23 ± 0.05	0.05 ± 0.01
Ser-emb 8 (N)	2	20.63 ± 0.89	1.95 ± 0.14	0.19 ± 0.01

Appendix F: Rotation diagram extinction and ortho-to-para ratio correction

The KP5 (Pontoppidan et al. 2024) extinction curve in the MIRI/MRS wavelength range used to derive A_K from the H_2 S(1) to S(4) lines is shown in Fig. F.1. We show an example of deriving the extinction correction for IRAS 23385+6053 aperture 1 and HH 211 aperture 8 in Fig. F.2, and an example of the correction for the ortho-to-para H_2 ratio in Figure F.3. The effect of extinction on the uncertainty in our warm H_2 and HD column densities and derived [D/H] are shown in Fig. F.4.

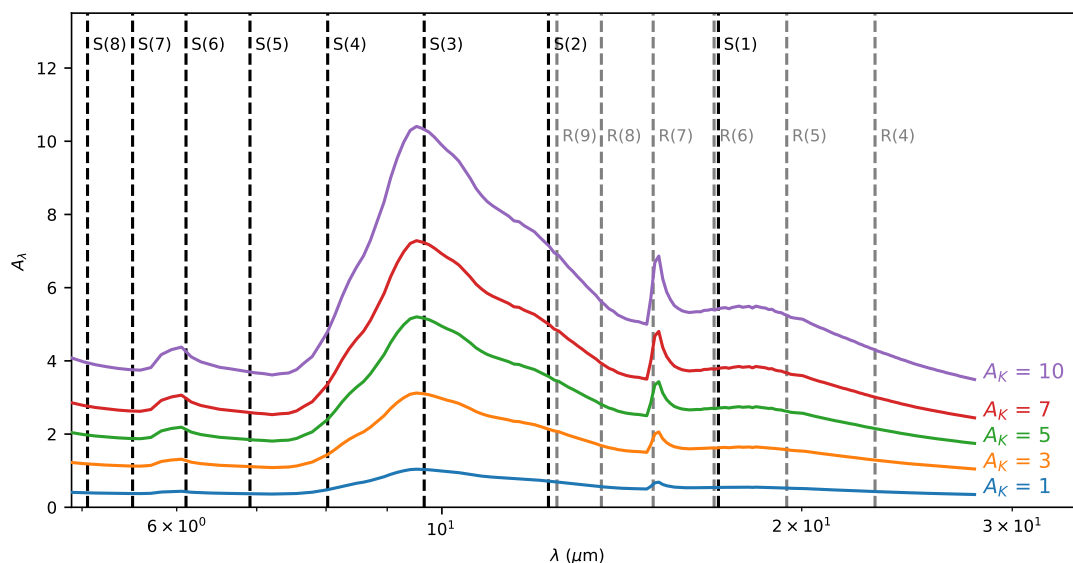


Fig. F.1. The KP5 (Pontoppidan et al. 2024) extinction curve for various values of A_K (solid lines) overlaid on the wavelengths of the H_2 and HD rotational transitions (dashed black and grey lines, respectively) analyzed in this work.

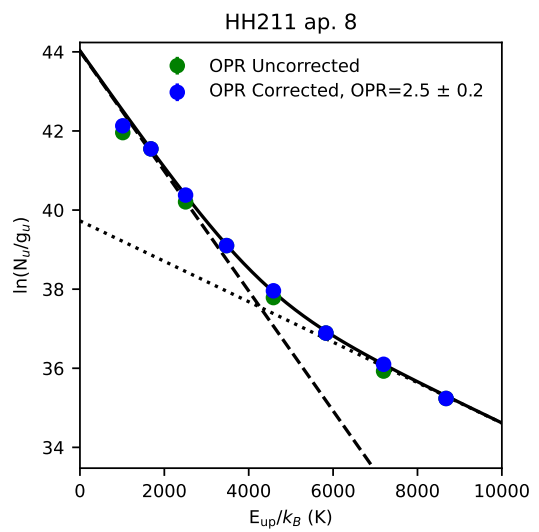
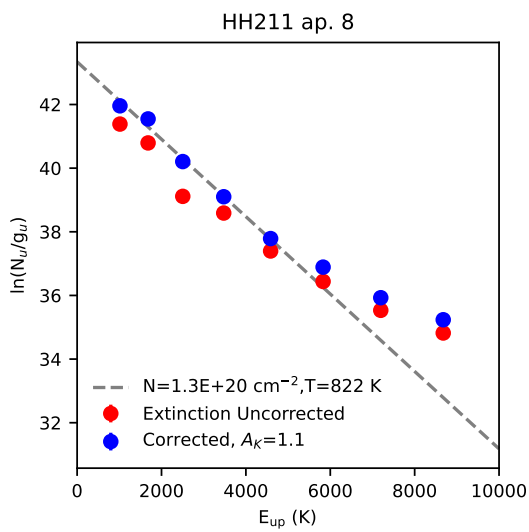
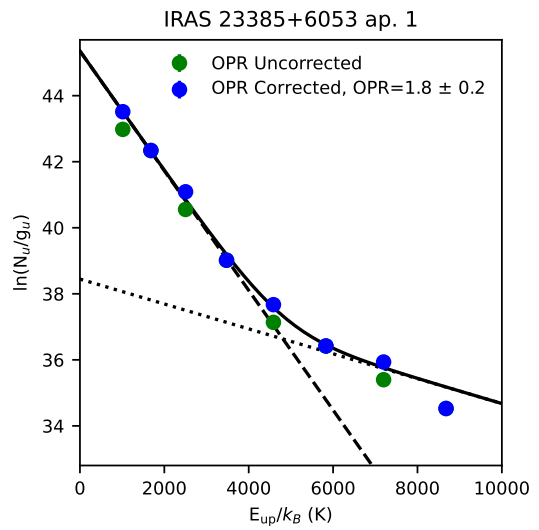
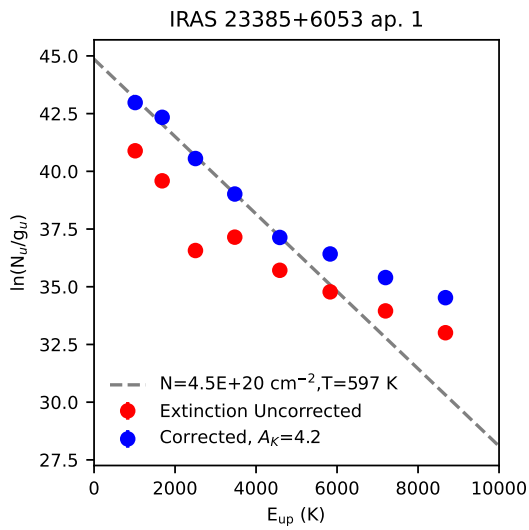


Fig. F.2. Rotation diagram for IRAS 23385+6053 aperture 1 and HH 211 aperture 8 with a fit to the S(1) to S(4) transitions to determine the extinction A_K . The uncorrected intensities are shown as red points, while the extinction corrected values are shown in blue. The dashed grey line shows the best fit of a single temperature component to the S(1) to S(4) transitions.

Fig. F.3. Example of the effect of correction for ortho-to-para H_2 ratio for IRAS 23385+6053 aperture 1 and HH 211 aperture 8. The effect on the H_2 rotation diagrams is shown before (green circles) and after (blue circles). The best-fit to the corrected data for the warm and hot H_2 components are overlaid as dashed and dotted lines, respectively.

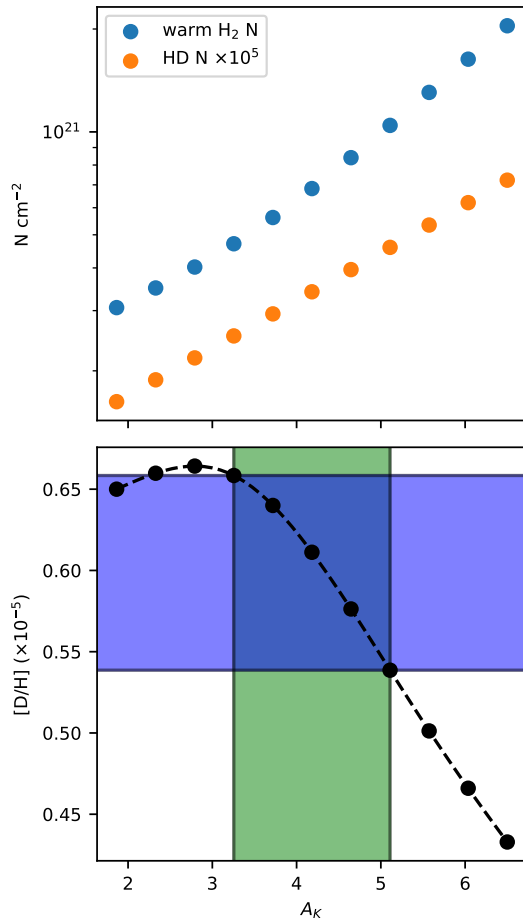


Fig. F.4. Example of the effect of extinction uncertainty on the derived column densities and [D/H] for IRAS 23385+6053 ap 1. *Upper panel:* Effect of varying extinction on derived column density for the warm H₂ component and HD. *Lower panel:* Effect of varying extinction on the derived [D/H]. The uncertainty in A_K from the single component fit to S(1)-S(4) transitions of H₂ is shown as the green shaded region, while the equivalent uncertainty in [D/H] is shown as the blue shaded region.

Appendix G: Rotation Diagram Fit Results

In table G.1, we provide the results of the rotation diagram fits for H₂ and HD to each aperture described in Section 3.3.

Table G.1. Rotation Diagram Fit Results.

Source	H ₂ N_{warm}	H ₂ T_{warm}	H ₂ N_{hot}	H ₂ T_{hot}	H ₂ OPR	HD N	HD T	A_K
G28-IRS2 ap. 1	3.05 ± 1.36 (20)	455 ± 52	4.68 ± 24.34 (17)	3000*	2.52 ± 0.77	< 1.20(16)	455 [†]	5.7 ± 0.1
G28-P1-A ap. 1	6.16 ± 3.13 (20)	466 ± 65	1.53 ± 2.81 (18)	3000*	1.66 ± 0.68	< 9.55(15)	466 [†]	6.0 ± 0.9
G31-A ap. 1	2.17 ± 1.24 (22)	395 ± 59	8.19 ± 23.30 (18)	3000*	1.02 ± 0.59	< 6.53(17)	395 [†]	9.3 ± 3.0
IRAS 18089-1732 ap. 1	1.52 ± 1.03 (22)	401 ± 52	9.51 ± 4.67 (18)	3000*	2.67 ± 0.59	< 8.88(16)	401 [†]	8.8 ± 2.4
IRAS 23385+6053 ap. 1	6.83 ± 0.99 (20)	552 ± 38	3.61 ± 5.13 (18)	2653 ± 2310	1.76 ± 0.17	3.41 ± 1.12 (15)	711 ± 59	4.2 ± 0.9
BHR71-IRS1 ap. 1	2.17 ± 0.59 (20)	853 ± 63	3.19 ± 15.63 (18)	3000*	2.67 ± 0.67	3.36 ± 0.85 (15)	849 ± 63	3.2 ± 0.7
BHR71-IRS1 ap. 2	5.99 ± 0.85 (19)	851 ± 65	2.56 ± 1.63 (18)	2747 ± 982	3.00 ± 0.25	5.15 ± 1.41 (14)	1043 ± 98	1.7 ± 0.4
BHR71-IRS1 ap. 3	3.66 ± 0.18 (19)	900 ± 35	1.90 ± 0.82 (18)	3000*	2.90 ± 0.14	3.76 ± 0.57 (14)	980 ± 41	1.1 ± 0.0
BHR71-IRS1 ap. 4	2.16 ± 0.10 (19)	659 ± 11	2.75 ± 0.87 (17)	3000*	3.00 ± 0.12	< 4.34(14)	659 [†]	1.2 ± 0.1
HH 211 ap. 1	1.52 ± 0.19 (20)	654 ± 28	6.13 ± 1.87 (18)	1463 ± 93	2.99 ± 0.09	1.62 ± 0.40 (15)	649 ± 40	1.3 ± 0.1
HH 211 ap. 2	1.48 ± 0.05 (20)	560 ± 20	7.72 ± 3.04 (18)	1160 ± 89	3.00 ± 0.13	2.09 ± 0.06 (15)	518 ± 4	1.2 ± 0.1
HH 211 ap. 3	1.41 ± 0.05 (20)	619 ± 28	3.95 ± 4.06 (18)	1392 ± 288	3.00 ± 0.14	2.04 ± 0.45 (15)	542 ± 27	1.2 ± 0.2
HH 211 ap. 4	6.47 ± 0.31 (19)	572 ± 13	9.24 ± 2.82 (17)	1551 ± 130	2.91 ± 0.08	< 6.19(14)	572 [†]	1.0 ± 0.2
HH 211 ap. 5	7.40 ± 1.43 (19)	623 ± 38	4.30 ± 6.80 (17)	2498 ± 1904	2.35 ± 0.15	< 5.17(14)	623 [†]	1.4 ± 1.1
HH 211 ap. 6	4.75 ± 0.25 (19)	552 ± 17	5.87 ± 3.74 (17)	1627 ± 342	2.76 ± 0.07	< 1.13(15)	552 [†]	0.9 ± 0.4
HH 211 ap. 7	1.75 ± 0.31 (21)	529 ± 51	3.22 ± 3.07 (19)	1696 ± 369	1.95 ± 0.37	3.62 ± 1.19 (15)	885 ± 67	1.7 ± 2.1
HH 211 ap. 8	2.13 ± 0.18 (20)	660 ± 50	8.97 ± 6.02 (18)	1956 ± 441	2.53 ± 0.21	5.71 ± 1.76 (14)	1271 ± 146	1.1 ± 0.8
HH 211 ap. 9	2.56 ± 0.54 (20)	639 ± 49	9.47 ± 4.96 (18)	2215 ± 620	2.08 ± 0.24	9.17 ± 3.33 (14)	1198 ± 132	1.5 ± 1.4
IRAS 4B ap. 1	3.12 ± 0.66 (21)	565 ± 43	3.48 ± 2.35 (19)	2249 ± 725	2.13 ± 0.18	3.05 ± 1.13 (15)	1690 ± 376	4.1 ± 1.5
IRAS 4B ap. 2	3.79 ± 1.00 (21)	552 ± 52	2.47 ± 1.67 (19)	2679 ± 1261	2.13 ± 0.26	3.84 ± 0.98 (15)	1694 ± 243	3.8 ± 1.5
L1448-mm ap. 1	1.70 ± 0.16 (20)	730 ± 33	2.08 ± 1.52 (18)	2620 ± 1181	3.00 ± 0.20	2.30 ± 0.30 (15)	811 ± 26	1.7 ± 0.2
L1448-mm ap. 2	1.01 ± 0.05 (20)	640 ± 12	8.74 ± 9.19 (17)	1891 ± 667	3.00 ± 0.14	1.87 ± 0.07 (15)	472 ± 3	1.3 ± 0.2
L1448-mm ap. 3	1.04 ± 0.03 (20)	649 ± 8	1.01 ± 0.42 (18)	1967 ± 334	2.98 ± 0.09	1.90 ± 0.24 (15)	481 ± 17	1.1 ± 0.0
L1448-mm ap. 4	4.09 ± 0.15 (19)	611 ± 14	6.46 ± 8.93 (16)	3000*	3.00 ± 0.08	< 4.61(14)	611 [†]	1.3 ± 0.0
Ser-emb 8 (N) ap. 1	4.01 ± 1.11 (20)	747 ± 213	2.16 ± 212.38 (19)	1519 ± 1826	1.39 ± 0.34	3.01 ± 0.53 (15)	749 ± 36	3.5 ± 1.9
Ser-emb 8 (N) ap. 2	5.35 ± 1.10 (20)	696 ± 91	4.14 ± 27.14 (18)	3000*	1.33 ± 0.23	2.50 ± 1.00 (15)	822 ± 100	3.2 ± 1.6

Numbers formatted as $a \pm b$ (c) indicate $(a \pm b) \times 10^c$. Error bars on column density and rotational temperature do not include uncertainty from extinction.

*Temperature of hot component reaches the fit limit of 3000 K and is highly uncertain.

[†]Temperature of HD assumed to be the same as warm H₂ for column density upper limit determination.